PAPER • **OPEN ACCESS**

Neuronal functional connectivity is impaired in a layer dependent manner near chronically implanted intracortical microelectrodes in C57BL6 wildtype mice

To cite this article: Keying Chen *et al* 2024 *J. Neural Eng.* **21** 036033

Journal of Neural Engineering

PAPER

Neuronal functional connectivity is impaired in a layer dependent manner near chronically implanted intracortical microelectrodes in C57BL6 wildtype mice

Keying Chen[1,2], **Adam M Forrest**[1,2], **Guillermo Gonzalez Burgos**[3] **and Takashi D Y Kozai**[1,2,4,5,6,*]

[1] Department of Bioengineering, University of Pittsburgh, Pittsburgh, PA, United States of America
[2] Center for Neural Basis of Cognition, Pittsburgh, PA, United States of America
[3] Department of Psychiatry, University of Pittsburgh, Pittsburgh, PA, United States of America
[4] Center for Neuroscience, University of Pittsburgh, Pittsburgh, PA, United States of America
[5] McGowan Institute of Regenerative Medicine, University of Pittsburgh, Pittsburgh, PA, United States of America
[6] NeuroTech Center, University of Pittsburgh Brain Institute, Pittsburgh, PA, United States of America
* Author to whom any correspondence should be addressed.

E-mail: TK.Kozai@pitt.edu

OPEN ACCESS

RECEIVED
6 November 2023

REVISED
22 April 2024

ACCEPTED FOR PUBLICATION
24 May 2024

PUBLISHED
7 June 2024

Keywords: brain circuit, LFP synchronization, visual cortex, neuroinflammation, brain-miachine interface, functional connectivity, decoder instability

Supplementary material for this article is available online

Abstract

Objective. This study aims to reveal longitudinal changes in functional network connectivity within and across different brain structures near chronically implanted microelectrodes. While it is well established that the foreign-body response (FBR) contributes to the gradual decline of the signals recorded from brain implants over time, how the FBR affects the functional stability of neural circuits near implanted brain–computer interfaces (BCIs) remains unknown. This research aims to illuminate how the chronic FBR can alter local neural circuit function and the implications for BCI decoders. *Approach.* This study utilized single-shank, 16-channel,100 μm site-spacing Michigan-style microelectrodes (3 mm length, 703 μm2 site area) that span all cortical layers and the hippocampal CA1 region. Sex balanced C57BL6 wildtype mice (11–13 weeks old) received perpendicularly implanted microelectrode in left primary visual cortex. Electrophysiological recordings were performed during both spontaneous activity and visual sensory stimulation. Alterations in neuronal activity near the microelectrode were tested assessing cross-frequency synchronization of local field potential (LFP) and spike entrainment to LFP oscillatory activity throughout 16 weeks after microelectrode implantation. *Main results.* The study found that cortical layer 4, the input-receiving layer, maintained activity over the implantation time. However, layers 2/3 rapidly experienced severe impairment, leading to a loss of proper intralaminar connectivity in the downstream output layers 5/6. Furthermore, the impairment of interlaminar connectivity near the microelectrode was unidirectional, showing decreased connectivity from Layers 2/3 to Layers 5/6 but not the reverse direction. In the hippocampus, CA1 neurons gradually became unable to properly entrain to the surrounding LFP oscillations. *Significance.* This study provides a detailed characterization of network connectivity dysfunction over long-term microelectrode implantation periods. This new knowledge could contribute to the development of targeted therapeutic strategies aimed at improving the health of the tissue surrounding brain implants and potentially inform engineering of adaptive decoders as the FBR progresses. Our study's understanding of the dynamic changes in the functional network over time opens the door to developing interventions for improving the long-term stability and performance of intracortical microelectrodes.

1. Introduction

Intracortical microelectrodes enable neural signal recording and electrical microstimulation in brain–computer interface (BCI) systems. These systems have applications in both basic understanding of normal brain activity as well as in clinical prostheses for restoring motor control and sensory perceptions [1–9]. For example, implanted microelectrodes can decode brain signals to drive prostheses in human patients [10], while electrical stimulation delivered by these devices helps modulate sensory perceptions in neural prosthetics [4, 11, 12]. Despite the promising role of intracortical microelectrodes, challenges remain regarding their sensitivity to record brain signals and regarding the stability of the microelectrode recordings, due to changes in network activity often attributed to 'plasticity' [13–20]. This challenge is represented by the difficulty in maintaining BCI decoders over time [3, 13, 14, 17, 21–24]. In addition, studies of rodents, non-human primates and human subjects have reported changes in signal quality possibly due to material and mechanical failures, such as material corrosion, degradation and/or tip breakage [25–27], or likely due to neuroinflammation and foreign body responses (FBRs) in surrounding tissue were reported [25, 28]. Despite knowing that implantation-related gliosis and neuronal loss contribute to the long-term decline in signal sensitivity [28, 29], there are still gaps in our understanding of how these factors specifically affect functional connectivity in brain circuits near implanted microelectrodes over time, separate from plasticity changes associated with learning.

Previous work showed that microelectrode implantation produces acute local inflammation that can affect the tissue homeostasis critical for information processing [28, 30]. The insertion of stiff, silicon-based microelectrodes disrupts the integrity of the blood-brain barrier, resulting in the infiltration of blood cells and plasma proteins [31–34]. This, in turn, recruits activated microglia and reactive astrocytes to migrate near the implanted microelectrode, leading to the formation of an encapsulating glial scar [35, 36]. The glial scar acts as a physical barrier for the exchange of ions and charged solutes between neurons and recording sites, consequently decreasing the signal-to-noise ratio thus affecting signal detectability [28, 37].

Moreover, microelectrode implantation may increase oxidative stress, pro-inflammatory cytokines, and glutamate in the local microenvironment of the electrode, affecting neuronal survival and synapse integrity [28, 38]. The consequent silencing or degeneration of nearby neurons may impair synaptic communication and neuronal activity [9, 31, 39, 40], likely contributing to diminished neural signal detection [9]. Additionally, oligodendrocytes and myelin, which are crucial for action potential conduction and to metabolically support axon function, are susceptible to injury during implantation, leading to progressive axonal degeneration and limited axonal regeneration capacity [41]. Thus, impaired oligodendrocyte and myelin function can also reduce the signals detected by the microelectrodes [42, 43].

The brain's information processing complexity arises from its diverse anatomical structures and functional connectivity [44]. Interconnected laminar structures with distinct local networks contribute to this complexity [45]. Visual cortical circuits are thought to process information sequentially, visual information entering Layer 4 (L4), progressing to Layers 2/3 (L2/3) for integration and complex processing, and finally reaching Layer 5/6 for its output [45] to subcortical structures like the hippocampus via white matter tracts [46]. Throughout these layers, a delicate balance between excitation and inhibition is vital for circuit function. Excitation/inhibition imbalance disrupts network stability leading to behavioral impairments [47]. Interestingly, microelectrode implantation injury increases expression of excitatory neurotransmission markers within the initial days, shifting towards increased expression of inhibitory neurotransmission markers after four weeks [31, 48]. These changes suggests that the circuit function near the microelectrode is altered during long-term implantation, possibly explaining, in part, why decoders need to be frequently updated [13, 14]. Exploring the evolution of functional connectivity within and across laminar structures after implantation may generate crucial information for understanding the chronic decline in performance of implanted microelectrode devices.

Here, we aimed to investigate the changes in functional network connectivity in the cortex and hippocampal CA1 during long-term microelectrode implantation. We used single-shank, 16-channel,100 μm site-spacing Michigan-style microelectrodes (3 mm length, 703 μm2 site area) spanning cortical layers and the hippocampal CA1 area to record spontaneous activity and activity evoked by a visual stimulus. Our extracellular recordings detected action potentials and local field potentials (LFPs) which reflect summed synaptic activity near the microelectrode [49–51]. We used cross-frequency LFP synchronization [52, 53], and action potential entrainment to LFP oscillatory activity [54], to quantify functional network connectivity. Our findings revealed depth-dependent changes in intralaminar network connectivity. Superficial Layers 2/3, rather than Layer 5, exhibited a rapid loss of detected activity for putative inhibitory neurons at 2 weeks post-implantation, whereas activity of putative excitatory neurons showed a continuous decline in firing rate without a loss of neuron detection. Furthermore, the impairment of cortical interlaminar connectivity

near the microelectrode was direction-dependent. During chronic implantation, excitatory connectivity decreased in the L2/3-to-L5 descending direction but was heightened in the reverse L5-to-L2/3 direction. These findings provide the first evidence for changes in functional network connectivity within and across laminar structures during long-term microelectrode implantation. Characterizing these changes may help elucidating the mechanisms underlying the decline in activity detected by chronically implanted microelectrodes and may facilitate the strategic development of adaptive BCI decoders for longitudinal tissue reactions.

2. Methods

2.1. Intracortical microelectrode implantation surgery

C57BL6 mice ($n = 8$, 4 males and 4 females, 11–13 weeks old, Jackson Laboratory, Bar Harbor, ME) were used in this study. A single shank 100 μm site spacing Michigan-style microelectrode (A16-3 mm-100-703-CM15, NeuroNexus, Ann Arbor, MI) was implanted in the left primary visual cortex of each animal. Surgical procedures were described in detail in previous publications [42]. Animals were anesthetized by intraperitoneally (I.P.) administration of xylazine (7 mg kg^{-1})/ketamine (75 mg kg^{-1}) mixture. After fixing the animal onto the stereotaxic frame, hair, skin, and connective tissue were removed above the implantation site. Vetbond was applied to dry the skull for dental cement adhesion. Three stainless steel bone screws (Fine Science Tools, British Columbia, Canada) were inserted, one over each of the motor cortices and one over the contralateral visual cortex, and then secured with a layer of dental cement. The electrode ground was wired to the bone screw over the ipsilateral motor cortex and the reference was wired to the bone screws over the contralateral motor and visual cortex. A 1 mm square craniotomy centered at 1.8 mm lateral to midline and 2.7 mm posterior to bregma was drilled. During the procedure, saline was periodically applied to prevent any thermal damage. Once the craniotomy was opened, a microelectrode was perpendicularly inserted at 15 mm s^{-1} until the tip of the microelectrode shank was sitting at 1600 μm below the surface. Subtle depth adjustments were manually made to confirm the last electrode site was inserted into the brain. The craniotomy was filled with sealant Kwik-Sil and then fully covered by dental cement to seal the headcap. Body temperature and oxygen flow were maintained over the entire surgery. The animal received post-operation analgesic treatment with ketofen (I.P., 5 mg Kg^{-1}) on the surgery day and the following two consecutive days. All experimental procedures were conducted following approval by the University of Pittsburgh, Division of Laboratory Animal Resources, and Institutional Animal Care and Use Committee in accordance with the standards for humane animal care as set by the Animal Welfare Act and the National Institutes of Health Guide for the Care and Use of Laboratory Animals.

2.2. Electrochemical impedance spectroscopy (EIS)

EIS of the implanted microelectrodes was conducted within a grounded Faraday cage. The impedance of the implanted microelectrodes was measured and verified to ensure device functionality prior to electrophysiological recording sessions. Animals were awake and head-fixed to a rotating platform while an Autolab potentiostat with 16-channel multiplexer (PGSTAT 128 N, Metrohm, Netherlands) was connected to the animal head-stage. Impedance spectra were obtained for each channel using a 10 mV sine wave spanning from 10 Hz to 32 kHz. The 1 kHz impedance value was reported for each animal for each day.

2.3. Electrophysiological recording

Animals were awake and head-fixed in a grounded Faraday cage to prevent environmental noise during electrophysiological recordings. Spontaneous recordings were conducted with animals sitting on a rotating platform in a dark environment. Visually evoked activity was measured with animals facing a monitor (V243 H, Acer. Xizhi, New Taipei City, Taiwan) to span a visual field of 60° wide and 60° high in the contralateral eye. The visual stimulation paradigm consisted of a drifting gradient of black and while solid bars (MATLAB Psychophysics toolbox) and was synchronized with the recording system (RZ2/PZ5, Tucker–Davis Technologies, Alachua FL) at 24 414 Hz. Details of this visual stimulation paradigm are described in [9, 42].

2.4. Electrophysiology data analysis

2.4.1. Depth alignment

Current source density (CSD) plots were used to identify the laminar depth along the implanted microelectrode shank. A 2nd order Butterworth filter at 0.4–300 Hz was applied to extract the LFP data stream. The CSD heatmap was plotted by computing the average evoked (stimulus-locked) LFP for each electrode site, smoothing the signal across all electrode sites (1-dimensional line fit), and then calculating the second spatial derivative. The CSD revealed a negative LFP polarity (inward current sink) within 100 ms after visual stimuli onset, which corresponded to the L4 cortical input. The cortical alignment corresponding to CSD-defined L4 was performed in each animal for each day.

2.4.2. Single-unit (SU) classification

The raw data was passed through a Butterworth filter from 0.3–5 kHz to produce spiking data. A threshold of 3.5 standard deviations below the mean was applied to isolate potential SU activity. Then

SU waveforms were manually sorted based on the quality and shape of neuronal waveforms, autocorrelograms, and peri-stimulus time histograms with 50 ms bins as previously described [9, 42]. The sorted SU waveforms were classified according to the spike width, defined as the latency between the trough and peak of the SU waveform [55]. The putative excitatory neurons were experimentally defined as the SU waveforms with spike width $\geqslant$0.41 ms, and putative inhibitory neurons were defined as the SU waveforms with spike width <0.41 ms.

2.4.3. Cross frequency LFP synchronization: phase amplitude coupling (PAC)

The functional network connectivity in the brain circuit was quantitatively described by the LFP oscillatory synchronization across different frequencies using the PAC measurements [52]. PAC defined the degree of LFP cross-frequency synchronization for how well the phase of low frequency oscillations (4–7.5 Hz) drives the amplitude of high frequency oscillations (30–90 Hz), which is calculated by the modulation index (MI).

The PAC MIwas calculated based on Kullback–Leibler (KL) formula [52, 56]. First, raw signal was bandpass filtered to specific LFP frequencies, *f*. The Hilbert transform was used to obtain the time series of the phase component from the slow frequency LFP activity in Channel *X*, which was denoted as $\Phi_X\ (t, f_X)$ (t = time, f_X = phase frequencies, 4, 4.5, 5, … 7.5 Hz). The time series of the amplitude component of the high frequency LFP activity in Channel *Y* was extracted by Morlet wavelet transform (5 cycles) for each frequency (f_Y = amplitude frequencies, 30, 30.5, 31, … 90 Hz), which was denoted as $A_Y\ (t, f_Y)$.

Next, the composite time series was constructed ($\Phi_X\ (t, f_X)$, $A_Y\ (t, f_Y)$) so that the amplitude of high frequency LFP oscillation in Channel *Y* was given at each phase of slow frequency LFP activity in Channel *X*. Then the phases $\Phi_X\ (t, f_X)$ were binned every 18° (N = total number of phase bins, 20), and the amplitude $A_Y\ (t, f_Y)$ at each phase bin (i) was averaged as $A_Y(t, f_Y)_{\Phi_X(t,f_X)}(i)$. Finally, the amplitude $A_Y(t, f_Y)_{\Phi_X(t,f_X)}(i)$ was normalized by the sum over all bins

$$P(i, f_X, f_Y) = \frac{A_Y(t, f_Y)_{\Phi_X(t,f_X)}(i)}{\sum_{k=1}^{N} A_Y(t, f_Y)_{\Phi_X(t,f_X)}(k)} \quad (1)$$

where $P(i,f_X, f_Y)$ represented the normalized amplitude distribution over phases. The normalized amplitude distribution $P(i,f_X, f_Y)$ would be uniform if there was no PAC between Channel *X* and *Y*. Thus, the level of deviation of from the uniform distribution indicated the existence of PAC, which was measured by joint entropy ($H\ (f_X, f_Y)$)

$$H(f_X,f_Y) = -\sum_{i=1}^{N} P(i,f_X,f_Y)\ \log P(i,f_X,f_Y). \quad (2)$$

The joint entropy reaches its maximum ($H_o = \log N^2$) when $P(i,f_X, f_Y)$ is uniform. Then, KL distance formula was applied to calculate the difference between $H\ (f_X, f_Y)$ and H_o. Thus, the MI of PAC was calculated by dividing the KL distance from the uniform distribution H_o.

$$\mathrm{MI}\,(f_X,f_Y) = \frac{H(f_X,f_Y) - H_o}{H_o}. \quad (3)$$

The range of MI is between 0 and 1. When Channel *X* = Channel *Y*, a larger MI value of PAC showed a stronger LFP synchronization coupling between the low frequency phase and the high frequency amplitude within the same layer, suggesting a higher activation level of the intralaminar network. When Channel *X* ≠ Channel *Y*, a larger MI value of PAC demonstrated an increased LFP synchronization coupling between the low frequency phase in the upstream layer and the high frequency amplitude in the downstream layer, reflecting an elevation in directional interlaminar connectivity.

2.4.4. Spike entrainment to LFP oscillation

As an alternative measurement for functional network connectivity, SU entrainment to LFP oscillation quantifies a directional coupling across different brain depths. Spike entrainment to LFP oscillation quantitatively describes a relationship between the timing of SU spikes and the phases of LFP [56]. The LFP oscillations are presumed to precisely organize the neuronal firing at a particular phase during communication between brain structures [54]. In this way, LFP oscillation has been considered as the oscillatory synchronized input to nearby neurons.

The MI of spike entrainment to LFP oscillation reflected the level of synchronization coupling between spike activity of the sorted SU and LFP oscillation at a specific frequency. The details of SU entrainment to LFP oscillation has been described previously [56]. First, raw signal of Channel *A* was bandpass filtered to specific LFP frequencies, *f* (see below for ranges). Then, a Hilbert transform was performed to extract the time series of the phase component from the LFP activity, which was denoted as $\Phi_A\ (t, f_A)$, where t represented the recording time and f_A represented phase frequencies (4, 4.5, 5, … 90 Hz). Then, the raw signal of Channel *B* was filtered from 0.3–5 kHz and a threshold of 3.5 standard deviations below the mean was applied to identify spike activity. The time series of spike activity was denoted as $S_B(t)$. If there is a spike at t_i, then $S_B(t_i) = 1$. Otherwise, $S_B(t_i) = 0$.

Next, the composite time series ($\Phi_A\ (t, f_A)$, $S_B\ (t)$) was constructed to give the occurrence of spike activity in Channel *A* at phases of Channel *B* LFP oscillation. Then, the phases $\Phi_A\ (t, f_A)$ were binned every 18° (N = total number of phase bins, 20), and the number of spikes $S_B\ (t)$ over each phase bin (j) was averaged (denoted as # spike (j)). Finally, the

probability distribution of spike activity over phases for each frequency f_A was calculated as

$$P(j,f_A) = \frac{\#\text{ spike}(j)}{\sum_{j=1}^{N}\#\text{ spike}(j)}. \quad (4)$$

Next, the joint entropy $H(f_A)$ was calculated as

$$H(f_A) = -\sum_{j=1}^{N} P(j,f_A)\ \log P(j,f_A). \quad (5)$$

Similar to PAC, the MI for spikes in channel B entraining to LFP oscillation in channel A was calculated using the KL equation:

$$\text{MI}(f_A) = \frac{H(f_A) - \log N^2}{\log N^2}. \quad (6)$$

The $\text{MI}(f_A)$ of spike entrainment to LFP for each SU was normalized to its maximum value across the frequency f_A. Then, a heatmap was constructed by the normalized MI of all sorted SU waveforms across frequencies to identify the LFP frequency range ($f_k = f_1, f_2, \ldots . f_n$) where the most SU waveforms were strongly entrained. If Channel A = Channel B, the MI measured the level of spike entrainment to the intralaminar LFP oscillation. If Channel $A \neq$ Channel B, the MI of spike entrainment to the interlaminar LFP oscillation reflects the directional network connectivity across cortical depth.

Once the LFP frequencies ($f_{n1} - f_{n2}$) were identified, the raw data in Channel A was bandpass filtered to $f_{n1} - f_{n2}$ frequencies. Then a Hilbert transform was applied to extract phase angles at each spike activity at Channel B. The directional statistics were performed using MATLAB Circular Statistics Toolbox. The mean resultant vector was measured, which reflected the mean phase angle of spike entrainment for that SU. The resultant vector length was reported to describe a spread of the individual phase angles about the mean angle. The sorted SU was considered entrained if the resultant vector length was significantly deviated from the uniformity threshold set by Rayleigh test ($p < 0.05$) [57]. Only the significantly entrained SU were statistically compared between different time periods of implantation.

2.5. Immunohistochemistry

16 weeks after microelectrode implantation, mice were perfused transcardially with 1x PBS and then 4% paraformaldehyde (PFA). The brain tissues were then postfixed with 4% PFA overnight at 4 °C, immersed in 30% sucrose for rehydration, and finally sectioned coronally into 25 μm slices until the probe trace was visualized. Standard immunohistochemical staining was performed. Following heat-induced antigen retrieval (0.1 M citric Acid, 0.1 M sodium citrate) and endogenous peroxidase blocking, the tissue was covered by 0.1% Triton-X with 10% normal goat serum in PBS at room temperature for 1 h. Primary antibodies GAD67 (1:500, Abcam, ab213508) and CamKiiα (1:100, Abcam, ab22609) were incubated overnight at 4 °C. Then the secondary antibodies (Nissl 435/455, Thermo Fisher, N-21479, donkey anti-rabbit 488, Abcam, ab150061, donkey anti-mouse 568, Abcam, ab175700, donkey anti-goat 647, Abcam, ab150135) in concentration of 1:500 were applied. After incubation, slides were washed with PBS and mounted with cover glass over Fluoromount-G media (SouthernBiotech, #0100-20). The 16-bit, 1024 × 1024 pixels (635.9 × 635.9 μm), 20x TIFF images were captured using a confocal microscope (FluoView 1000, Olympus, Inc., Tokyo, Japan) system with an oil-immersive objective lens.

2.6. Statistics

Significant differences between visual evoked and spontaneous conditions were assessed using a linear mixed effect model to account for repeated measures. The model applied a restricted cubic spline with four knots at the 5th, 35th, 65th, and 95th percentiles of the data for nonlinear fit. In this model, the time and the condition-by-time interaction are fixed effects. The group-wise difference was significant if the 95% confidence intervals (1.96 times the standard error of the model fits) were not overlapping based on a likelihood test. The significant changes in metrics over time were assessed using a one-way ANOVA with Tukey post hoc tests. The Repeated Measures ANOVA was applied to detect significance in angular measurements across different implantation stages, using the Watson–Williams test for the resultant mean entrainment angles and the Kuiper test for the distribution of entrainment angles.

3. Results

3.1. Layer-specific characteristics of classified SU firing activity

Given the distinct patterns of anatomical connectivity across cortical layers and hippocampus, we first examined the firing activity of putative neuronal subtypes at various depths. Sixteen-channel microelectrodes were perpendicularly inserted into the brain through the primary visual cortex and to a depth of 1.6 mm so that the tip reached hippocampus CA1 (figure 1(A)). No material failure or mechanical failure was observed in these implanted microelectrodes, and the electrochemical properties of the implanted microelectrodes remained stable over time as indicated by the non-significant differences in channel-averaged impedance (figure 1(B), One-way ANOVA, $p = 0.569$). The recorded SU spikes are widely acknowledged to represent action potentials generated by individual neurons [58, 59]. The SU yield was determined to assess the availability of active neuronal sources in proximity to the chronically implanted microelectrode (supplementary figure

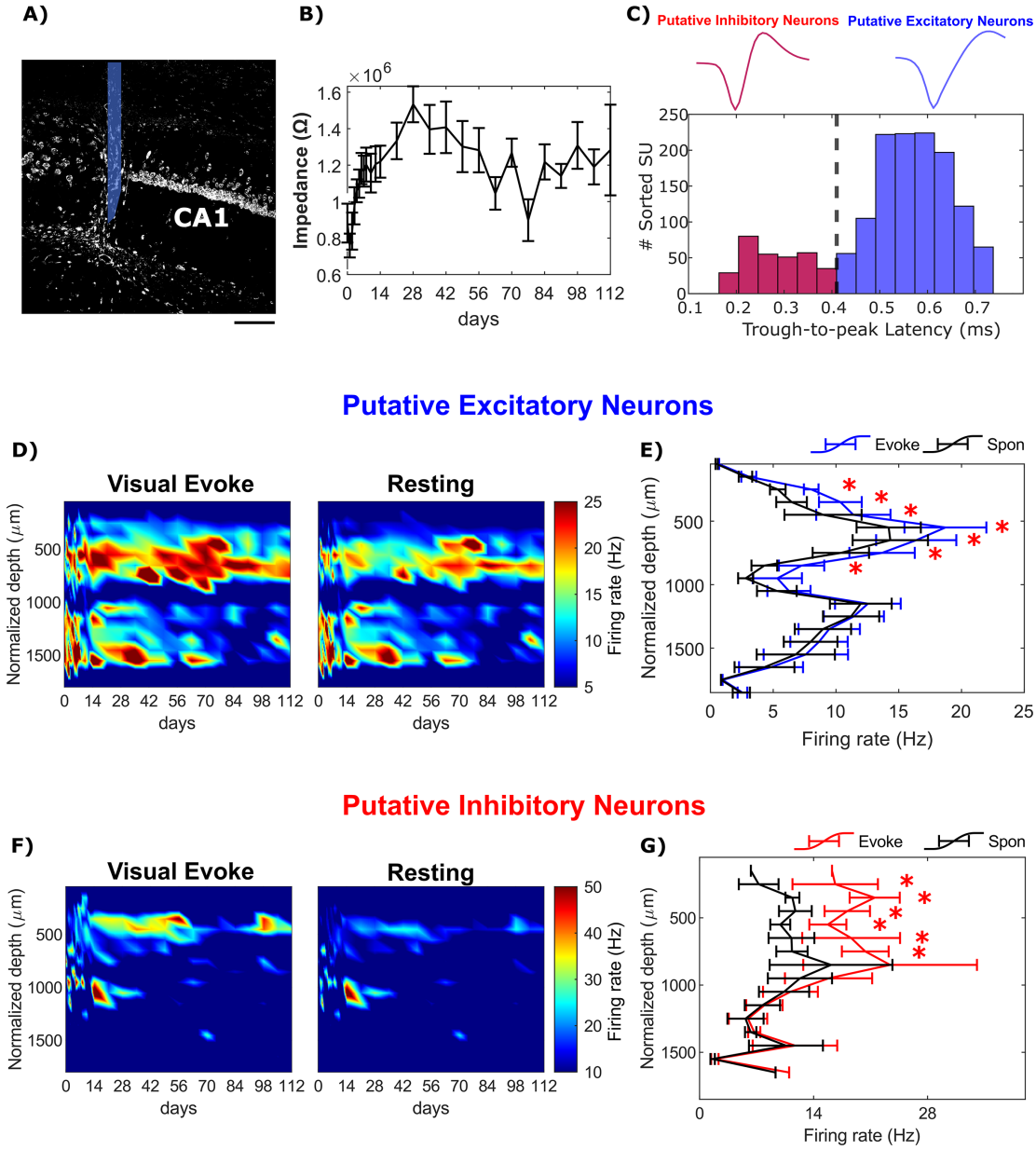

Figure 1. Visual stimulation activates distinct neuronal subtypes in depth-dependent manner. (A) Representative Nissl+ neuronal soma staining of the hippocampal CA1 reveals the probe trace with the tip positioned below CA1. The location of the probe is labeled in blue. Scale bar = 100 μm. (B) Impedance at 1 kHz was averaged across channels was stable over time (One-way ANOVA, $p = 0.569$). (C) Top: Example of a representative narrow waveform classified as a putative inhibitory neuron (left) and representative wide waveform sorted as a putative excitatory neuron (right). Bottom: single-units (SUs) were classified based on trough-to-peak (TP) latency, which followed a bimodal distribution. SU waveforms with TP latencies less than 0.41 ms were classified as putative inhibitory neurons (red), while SU waveforms with TP latencies greater than 0.41 ms were classified as putative excitatory neurons (blue). (D) SU firing rate heatmaps of putative excitatory neurons during visual evoked responses (left) and resting state (right) as a function of time and depth. (E) The depth profile of putative excitatory firing rate showed a significant increase in firing rate in the cortex during visual stimulation (Linear mixed effect model with likelihood ratio test, $p = 0.078$). (F) SU firing rate heatmaps of putative inhibitory neurons during visual evoked responses (left) and resting state (right) as a function of time and depth. (G) Putative inhibitory neurons exhibited a significant increase in firing rate in the cortex (peaked in L2/3) during visual stimulation compared to the resting state (Linear mixed effect model with likelihood ratio test, $p = 7.27 * 10\text{^}(-5)$). Asterisks (*) indicate non-overlapping 95% confidence intervals between visual evoked responses and resting state at each time point, determined using a linear mixed-effects model with likelihood ratio test.

1(A)). The SU yield in cortex remained relatively stable up to 12 weeks post-implantation, after which it began to decline gradually over time. Notably, the SU yield in the hippocampal region was consistently lower compared to that in the cortex. We further classified these SU waveforms into putative excitatory or inhibitory neurons to gain detailed insights into firing activity within neuronal networks at different depths using trough-to-peak latency of all SU waveforms [55, 56, 60]. A bimodal distribution was observed with narrow waveforms peaking at 0.25 ms, consistent with previous observations for inhibitory neurons [37, 38] and the wide waveforms peaking at 0.54 ms, corresponding to excitatory neurons [61]. Using a

threshold of 0.41 ms, we identified a total of 440 waveforms as putative inhibitory neurons and 1476 waveforms as putative excitatory neurons in awake mice over the entire 16 week implantation period (figure 1(C)). We also investigated the detectability of putative excitatory and inhibitory neurons across different depths and over time. The majority of the SUs detected were classified as putative excitatory neurons, constituting 78.46% ± 2.37% in the cortex and 89.73% ± 3.01% in the hippocampus (supplementary figure 1(B)). The yield of putative excitatory neurons remained relatively stable over time. However, we observed a chronic reduction in the detectability of putative inhibitory neurons, particularly in the cortical region. Additionally, there was a gradual decline in the percentage of putative inhibitory neurons relative to the total number of sorted SUs over time (supplementary figure 1(C)). These observations suggest that the reduced SU detectability near the chronically implanted microelectrode is likely due to a decreased detection of putative inhibitory neurons compared to putative excitatory neurons.

The firing rate of putative excitatory neurons with wide spike waveform exhibited two distinct peaks along the depth axis (figure 1(D)). The first peak, with a firing rate of 18.72 ± 3.26 Hz, was observed at ∼600 μm depth corresponding to L5 neurons. This finding is consistent with previous observations of high firing rates of large L5 pyramidal neurons in cortex [62] (figure 1(E)). The second peak, with a firing rate of 12.54 ± 2.62 Hz, was observed at ∼1,200 μm depth, likely corresponds to pyramidal neurons in CA1 stratum pyramidale (SP) characterized by dense cell bodies (figures 1(D) and (E)). This firing rate was relatively higher than the firing rate of CA1 neurons as reported [63], which is likely due to multiple neurons being classified under the same waveform in extracellular recording conditions. During visual stimulation, the firing rate of putative excitatory neurons in visual cortex significantly increased compared to resting state within the depth range of 250–850 μm ($p = 0.078$, likelihood ratio test with non-overlapping 95% confidence intervals). Notably, the largest increase, approximately 31%, was observed in Layer 4 (L4), which is the primary target of excitatory thalamic afferents conveying information from the visual stimuli [64, 65]. In contrast, in the hippocampus, the visually evoked increase in the firing rate of putative excitatory neurons was limited to only around 5%, showing that visual stimulation with a drifting-bar gradient had a relatively weaker effect in activating the hippocampus CA1 region near the implanted microelectrode. Taken together, the firing rate of putative excitatory neurons displayed a significant increase in L4 during visual stimulation, but limited effects in the hippocampus CA1 region near the microelectrode.

In contrast to putative excitatory neurons, putative inhibitory neurons with narrow spike waveform from visual cortex displayed consistent firing rate across cortical depth and exhibited a higher overall firing rate. (Figure 1(F); mean firing rate of putative excitatory neurons: 11.79 Hz, mean firing rate of putative inhibitory neurons: 18.55 Hz). The increase in putative inhibitory firing rate during visual stimulation was statistically significant at depths ranging from 150–750 μm below the surface (Linear mixed effect model with likelihood ratio test, $p = 7.27 * 10\text{^}(-5)$). However, in the hippocampus, the increase was only 3% compared to resting state (figure 1(G)). The peak increase in putative inhibitory firing rate, approximately 89% higher than resting state, occurred in L2/3. Given that GABAergic interneurons regulate signal flow and shape network dynamics [66, 67], the substantial elevation in putative inhibitory firing rate in L2/3 indicates is consistent with the critical contribution of interneuron-mediated processes in this layer, such as lateral inhibition, in cortical information processing. In summary, the putative excitatory and inhibitory neuron subtypes in visual cortex exhibited different depth profiles of firing rate during visual stimulation. Whereas the input layer L4 experienced a prominent increase in excitatory neuron activity, L2/3 showed the strongest inhibitory network activation. Interestingly, the hippocampal CA1 region did not show a significant increase in firing activity for either putative neuronal subtypes during passive drifting-bar gradient visual stimulation.

3.2. Patterns of change in cortical laminar networks near the chronically implanted microelectrode

The depth profile of the firing rate of putative neuronal subtypes provides insights into the interconnectedness of cortical laminar structures, which exhibit distinct network functionality for information processing. Our objective was to gain better understanding of the changes in functional network connectivity in cortex over long-term microelectrode implantation. To achieve this we first examined specific cortical intralaminar networks involved in visual processing. To evaluate the impact of long-term microelectrode implantation on functionality of intralaminar networks, we examined the LFP cross-frequency synchronization, SU firing rates of putative neuron subtypes, and spike entrainment to intralaminar LFP. SU spiking activity specifically requires the involvement of neurons in close proximity to the electrode site [68–70] (usually within 80–140 μm). Studying LFP cross-frequency synchronization allows us to gauge the level of network activation over a broader distance, while changes in spiking rate can provide insights into the function of local networks surrounding the implanted microelectrode within about 100 μm. Since LFP oscillations are understood to reflect synchronized input to nearby populations of neurons [54, 71], analyzing spike entrainment of individual neurons to the population's intralaminar

LFP oscillation informs us about the responsiveness of the individual neurons to the surrounding network. By employing these three measurements, we aim to uncover a novel perspective on potential changes in network functionality near the chronically implanted microelectrode.

3.2.1. Stable excitatory connectivity in L4

We started our investigation in L4 as it is the primary input-receiving layer in cortex. To investigate the functional connectivity within the intralaminar network of L4 during visual processing, we examined the LFP cross-frequency synchronization between theta (4–7.5 Hz) and gamma (30–90 Hz) oscillations within depths corresponding to L4. This theta–gamma coupling has been recently identified as a critical neural coding mechanism in cognition [72], where the phase of theta oscillation is strongly coupled with the gamma power during network activation [73]. To quantitatively assess the PAC between theta and gamma oscillatory activity, we calculated the MI for LFP synchronization. The MI measures the strength of synchronization between the low-frequency phase and high-frequency amplitude, with a range between 1, indicating strong LFP synchronization, and 0, indicating loss of synchronization. Our results revealed a robust PAC relationship between the phase around ∼4 Hz and the amplitude in the 80–90 Hz range during visual evoked recordings (figure 2(A)). Furthermore, we observed that the MI value during visual stimulation consistently remained significantly elevated compared to the MI during resting state throughout the entire 16 week chronic implantation period (figure 2(B), linear mixed effect model with likelihood ratio test, $p = 1.45 * 10\text{^}(-7)$). Aditionally, there were no significant differences in MI values during visual stimulation across different time points (One-way ANOVA, $p = 0.361$). Our LFP findings within L4 indicate that the intralaminar network in this layer is consistently activated near the chronically implanted microelectrode in response to visual stimuli.

Then, we examined the firing rate of individual L4 SU waveforms near the microelectrode. The firing rate of putative excitatory neurons in L4 showed a noticeable increase during visual stimulation compared to the resting state, indicating their involvement in L4 activation (figure 2(C)). Moreover, the firing rate of putative excitatory neurons in L4 remained stable over time (Two-way ANOVA with Tukey post hoc, $p = 0.307$). In the case of putative inhibitory neurons in L4, visual stimulation led to a significant elevation in their firing rate compared to the resting state (figure 2(D), two-way ANOVA with Tukey post hoc, $p = 0.0034$), emphasizing the crucial role of inhibitory neurons in L4 activation. However, starting from week 5 post-implantation, there was a decline in the detection of sufficient putative inhibitory neurons in L4. It is possible that local interneurons detected as the putative inhibitory neurons here became silent or injured due to microelectrode implantation. However, those interneurons in distal regions that are outside the detection range of the microelectrode are likely still functioning and generate the theta and gamma rhythms (figures 2(A) and (B)).

Next, we investigated whether the activity of individual neurons during the intralaminar LFP oscillatory input was influenced by the chronic implantation injury. While the overall firing rate of L4 putative excitatory neurons remained stable over time, it was important to determine if these neurons were able to effictively synchronize (phase lock) their activity with LFP oscillations. We first focused on the entrainment of L4 putative excitatory neurons to slow 2–7.5 Hz LFP oscillations. Remarkably, a substantial portion (nearly 42%) of L4 putative excitatory neurons exhibited a significant entrainment to this slow 2–7.5 Hz LFP oscillation (Rayleigh test, $p < 0.05$; figure 2(E)). These neurons consistently aligned their spiking activity with the bottom of the slow oscillation, and their distribution variability of entrainment phases and mean preferred phase did not exhibit significant differences over time (figure 2(F); Watson–William's test, $p > 0.05$; Kuiper test, $p > 0.05$). Thus, the spike timing of L4 excitatory neurons consistently synchronized with the trough of the slow oscillation throughout the entire chronic implantation period, suggesting stable activity during LFP oscillations of L4 excitatory neurons.

We further investigated the activity of L4 putative inhibitory neurons by examining their spike entrainment to intralaminar LFP. Our analysis revealed that 53.3% of L4 putative inhibitory neurons exhibited significant entrainment to the intralaminar 2–7.5 Hz oscillation, and 20% showed significant entrainment to 80–90 Hz gamma oscillation (figure 2(G), Rayleigh test, $p < 0.05$). However, unlike putative excitatory neurons, the L4 putative inhibitory neurons displayed significant changes in distribution variability of entrainment phases of slow 2–7.5 Hz oscillation during the early chronic stages (3–8 weeks) compared to the first two weeks (figure 2(H)); Kuiper test, $p < 0.05$). This significant change in spike-LFP coupling of L4 putative inhibitory neurons suggests an early deficit in the ability of L4 inhibitory neurons to respond to intralaminar slow oscillations. On the other hand, L4 putative inhibitory neurons exhibited no significant differences in mean phase or phase distribution variability of 80–90 Hz gamma oscillation across different implantation stage (figure 2(I); Watson–William's test, $p > 0.05$; Kuiper

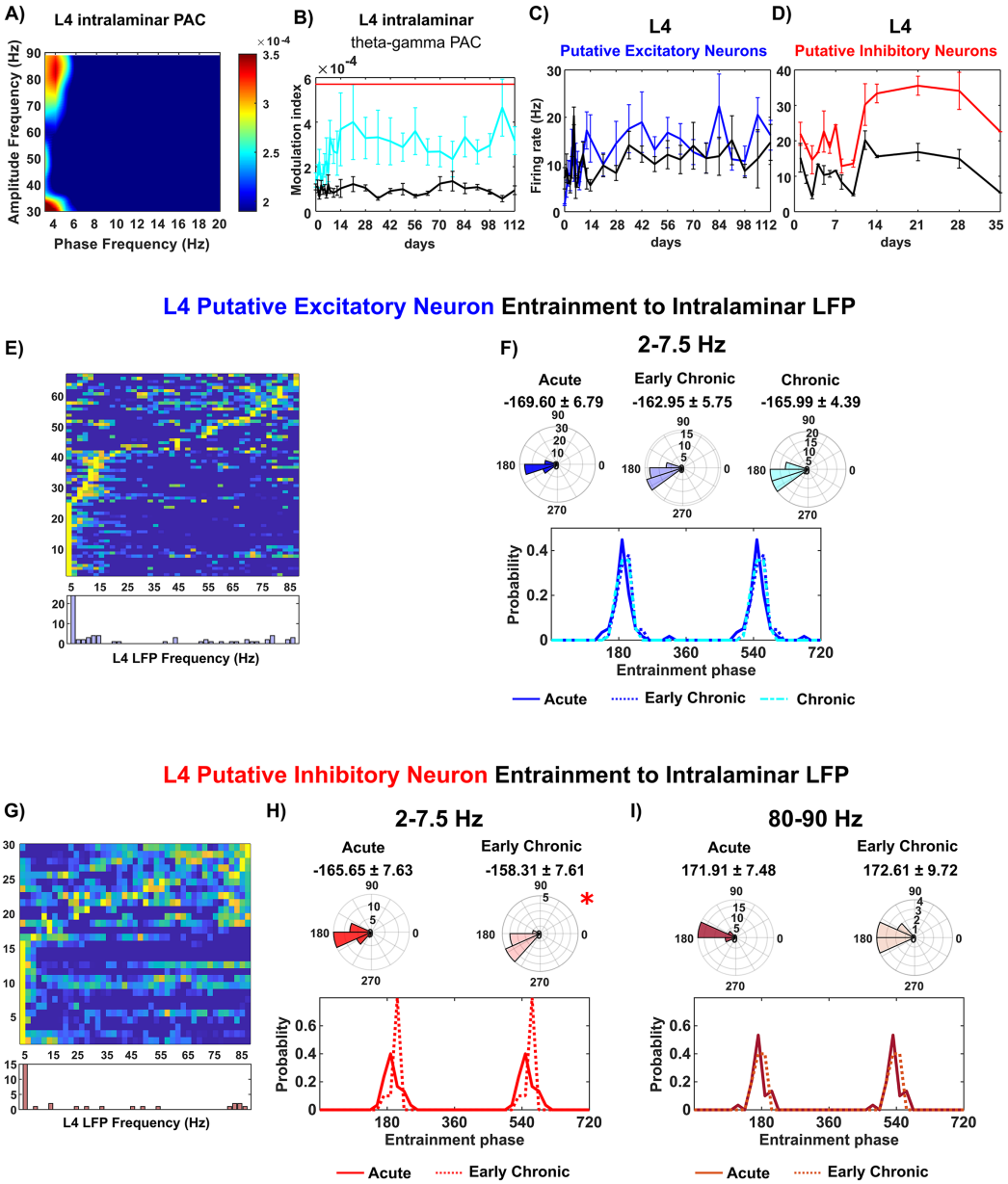

Figure 2. L4 maintained a stable excitatory connectivity over time but experienced loss of putative inhibitory neuron activity 5 weeks post implantation. (A). Comodulogram displays the Modulation Index (MI) of phase frequency (2–20 Hz) with the amplitude frequency (30–90 Hz) in L4. Note: strong coupling is observed between ∼4 Hz phase and the ∼80–90 Hz amplitude during visual stimulation. (B). The MI index of the 4 Hz theta phase coupling with 80–90 Hz gamma amplitude is significantly higher during visual stimulation (cyan) compared to the resting state (black) throughout the entire 16 week microelectrode implantation period. The red bar indicates significance of this difference across all time points (Linear mixed effect model with likelihood ratio test, $p = 1.45 * 10\ \hat{}(-7)$). (C). The firing rate of putative excitatory neurons during visual evoked activity (blue) and resting state (black) is plotted over time (Two-way ANOVA with Tukey post hoc, $p = 0.307$). (D). The putative inhibitory firing rate is significantly higher during visual stimulation (red) compared to resting state (black) but detection of inhibitory neurons is lost after week 5 post-implantation (Two-way ANOVA with Tukey post hoc, $p = 0.0034$). (E). L4 putative excitatory neurons exhibit entrainment to intralaminar slow oscillation. The top panel shows the normalized spike-LFP entrainment MI across frequencies for each L4 putative excitatory neuron with a Rayleigh test p-value < 0.05. The bottom panel displays a histogram indicating that a group of putative excitatory neurons are predominantly modulated by the L4 intralaminar slow oscillation (2–7.5 Hz). (F). The entrainment phase angles of L4 putative excitatory neurons to intralaminar slow 2–7.5 Hz oscillation are shown in a polar histogram (top) and line plot (bottom). The mean phase angle of entrained L4 excitatory neurons is reported for the acute (0–2 weeks), early chronic (3–8 weeks), and chronic (9–16 weeks) implantation periods (Watson–William's test, $p = 0.142$; Kuiper test, $p > 0.1$). (G) The top panel demonstrates the normalized spike-LFP entrainment MI value for each significantly entrained putative inhibitory neuron (Rayleigh test p-value < 0.05) across frequencies. The bottom panel shows a histogram indicating that putative inhibitory neurons are primarily entrained to two frequencies: the slow 2–7.5 Hz oscillation and the high 80–90 Hz frequency. The polar histograms and line plots illustrate the entrainment phase of L4 putative inhibitory neurons to the slow 2–7.5 Hz frequencies (H), acute vs early chronic: Watson–William's test, $p = 0.279$; Kuiper test, $p < 0.02$) and the 80–90 Hz high frequencies (I), acute vs early chronic: Watson–William's test, $p = 0.725$; Kuiper test, $p > 0.1$) of L4 intralaminar LFP at the acute (0–2 weeks) and early chronic (3–8 weeks) implantation stages. Spike-LFP entrainment analysis was not performed during the chronic (9–16 weeks) stage due to the loss of L4 putative inhibitory neuron detection. The red bar indicates non-overlapping 95% confidence intervals between visual evoked responses and resting state at each time point. The asterisk (*) indicates significant differences between the phase angular distribution in terms of resultant mean angles (Watson–Williams test), distribution variability (Kuiper test), or both.

test, $p > 0.05$). The firing activity of L4 putative excitatory neurons and their relationship with oscillatory LFP input remained preserved over time, indicating the robustness of the L4 intralaminar excitatory network during the chronic 16 week implantation period. However, the putative inhibitory neurons in L4 exhibited an early deficit in spike entrainment to slow oscillation, suggesting L4 inhibitory neurons experienced an impairment in synchronization of firing activity to surrounding oscillation. This dysregulation was followed by a detection loss of L4 putative inhibitory neurons, the temporal sequence indicating an early dysfunctionality of these neurons near the chronically-implanted microelectrode. Taken together, these results indicate that the primary input-receiving L4 maintained the excitatory functional connectivity yet experienced a reduction inintralaminar inhibitiory activity.

3.2.2. Rapid decline in L2/3 network activity

In the visual cortex, it is well-accepted that after most of the sensory information enters L4, it is then transmitted to L2/3, and finally to L5/6 [74]. Given the gradual loss in the detection of local inhibitory neuronal activity in L4, we then asked whether, when, and how the activity of the downstream L2/3 intralaminar network changes during the 16 week microelectrode implantation period. First, we observed the depth distribution of sinks and sources in the CSD during visual stimulation (supplementary figure 2), which provides an overview of changes in information transmission at various depths within V1 over time. Visual stimulation led to a stable sink at Layer IV (L4), supporting our results shown in figure 2. These results indicate that afferent activation from the subcortical lateral geniculate body to the cortex is minimally affected by implantation injury. While the sink-source pair in Layers V/VI (L5/6) appeared consistent throughout the implantation period, the source in the superficial layers corresponding to L2/3, paired with the L4 sink, gradually diminished. This decline in the L2/3 source likely reflects impaired information processing from L4 to L2/3 in the neural circuitry near the implanted microelectrode. Next, we performed an analysis of LFP cross-frequency synchronization, which was focused on the coupling between theta phase and gamma amplitude in L2/3 LFP oscillations. The MI of the L2/3 theta-gamma PAC demonstrated a strong coupling between ∼5 Hz theta phase and ∼65–90 Hz gamma amplitude during visual stimulation (figure 3(A)). In comparing the visually-evoked responses with the resting state, we observed significant differences in MI values. This underlines that visual stimulation results an increased LFP synchronization in L2/3 and thus indicates an enhanced intralaminar network connectivity relative to resting state. Interestingly, we observed a gradual decline in the MI value of L2/3 theta-gamma PAC during visual stimulation, reaching a comparable level to the resting state at week 8. However, starting from week 13 post-implantation, the MI values significantly increased again (figure 3(B), linear mixed effect model with likelihood ratio test, $p = 1.99\ ^*10\hat{}(-12)$). The initial decline in MI during visual stimulation suggests a functional impairment in the L2/3 intralaminar network near the microelectrode, while subsequent increase in MI values suggests a chronic enhancement. This longitudinal changes in L2/3 intralaminar connectivity potentially indicates a remodeling process of functional network connectivity. These findings shed light on the dynamic changes in the L2/3 intralaminar network near the chronically implanted microelectrode. The impairment followed by potential remodeling suggests a complex interplay between the microelectrode and the functional network connectivity in L2/3.

The firing activity of both L2/3 putative excitatory and inhibitory neuronal subtypes exhibited a progressive decline. Specifically, the firing rate of L2/3 putative excitatory neurons showed a substantial declined over the 16 weeks post-implantation period, with a significant reduction observed at week 16 compared to weeks 1–8 (figure 4(C), one-way ANOVA with Tukey post hoc, $p < 0.01$). This impaired firing activity indicates progressive impairment of the L2/3 excitatory network. Furthermore, L2/3 putative inhibitory neurons displayed a significant increase in visually evoked firing rate compared to resting state (figure 3(D), linear mixed effect model with likelihood ratio test, $p = 7.82\ ^*\ 10\hat{}(-6)$). However, the detection of sufficient L2/3 putative inhibitory neurons was not possible after week 2 post-implantation, suggesting that inhibitory neurons in L2/3 were susceptible to acute implantation injury. This dysfunction of L2/3 putative excitatory and inhibitory neuronal firing activity indicates that the local L2/3 network adjacent to the microelectrode was compromised, which is further supported by the evidence of immunohistochemical staining (figure 8).

Furthermore, our analysis of spike entrainment to the LFP in L2/3 sheds light on the changes of neuronal communication near the microelectrode. Specifically, putative excitatory neurons in L2/3 exhibited a preference for entrainment to intralaminar 2–7.5 Hz theta frequencies (19.7%) as well as 60–90 Hz gamma frequencies (36%) (figure 3(E)). However, these neurons were unable to maintain an organized distribution of entrainment phase to either frequency band. Significant differences were detected in both the mean as well as the variability of entrainment phase angles during the early chronic phase (3–8 weeks) and chronic phase (9–16 weeks) compared to the acute phase (0–2 weeks) (figure 3(F), Watson–William's test $p < 0.05$; Kuiper test, $p < 0.05$). Additionally, the mean phase of L2/3 putative excitatory spike entrainment to intralaminar gamma oscillation (60–90 Hz) showed a significant shift in the mean phase since early chronic phase (3–8 weeks) (figure 3(G),

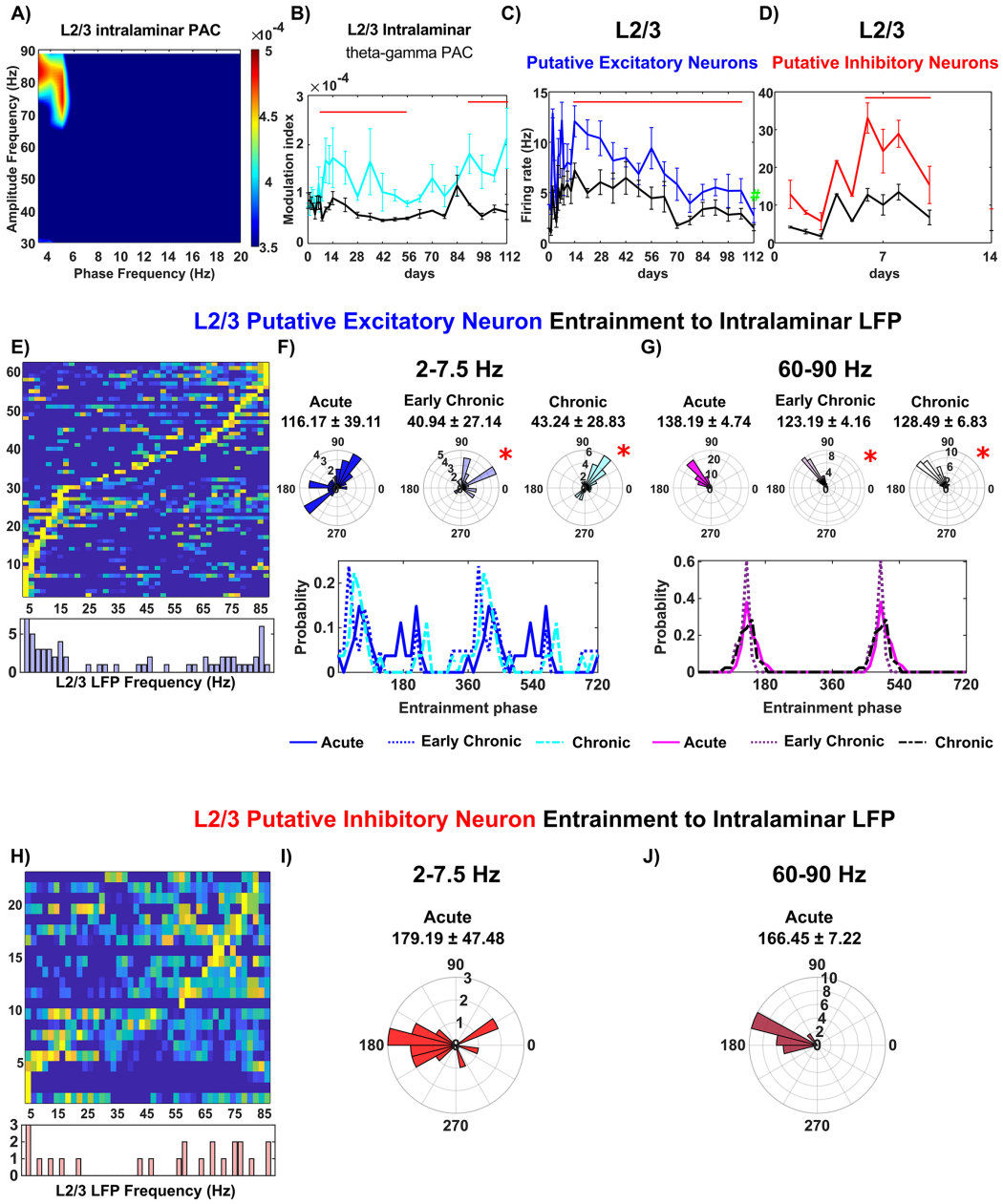

Figure 3. Electrode implantation leads to a loss of L2/3 putative inhibitory neurons and a significant reduction in the firing rate of putative excitatory neurons. (A) Comodulogram of L2/3 intralaminar theta-gamma modulation index (MI) showing the phase frequency (2–20 Hz) with the amplitude frequency (30–90 Hz). Visual evoked responses induce a robust coupling between ∼5 Hz phase and the ∼65–90 Hz amplitude. (B) Time series of L2/3 theta–gamma phase-amplitude coupling (PAC) during visual evoked responses (cyan) and resting state (black) over time (Linear mixed effect model with likelihood ratio test, $p = 1.99 * 10\hat{}(-12)$). (C) Putative excitatory neurons in L2/3 experience a substantial decrease in firing rate during visual evoked activation. Visual evoked responses significantly increase the firing rate of putative excitatory neurons compared to the resting state (One-way ANOVA with Tukey post hoc, $p < 0.01$). (D) Putative inhibitory neurons in L2/3 significantly increase their firing rate during visual evoked responses compared to the resting state, but the detection of these units is lost after week 2 post-implantation (Linear mixed effect model with likelihood ratio test, $p = 7.82 * 10\hat{}(-6)$). (E) Putative excitatory neurons in L2/3 show entrainment to intralaminar slow and fast oscillations. The top panel shows normalized spike-LFP entrainment modulation indices (MI) across frequencies for each putative excitatory neuron in L2/3 with a Rayleigh test p-value < 0.05. The bottom panel presents a summary histogram indicating that a cluster of putative excitatory neurons in L2/3 is mostly entrained to intralaminar slow oscillations (2–7.5 Hz), while the other cluster is mostly entrained to high-frequency oscillations (60–90 Hz). (F) Distribution of phases of putative excitatory neurons in L2/3 significantly entrained to 2–20 Hz slow frequency oscillations at three different implantation stages (acute vs early chronic: Watson–William's test, $p = 9.16 * 10\hat{}(-4)$; Kuiper test, $p > 0.1$; acute vs chronic: Watson–William's test, $p = 0.001$; Kuiper test, $p < 0.02$). The top panel shows a polar histogram with the mean phase reported, while the bottom panel displays a line plot. (G) Distribution of phases of putative excitatory neurons in L2/3 significantly entrained to 60–90 Hz high-frequency oscillations at different implantation stages (acute vs early chronic: Watson–William's test, $p = 3.56 * 10\hat{}(-5)$; Kuiper test, $p < 0.02$; acute vs chronic: Watson–William's test, $p = 0.015$; Kuiper test, $p > 0.1$). The top panel shows a polar histogram, and the bottom panel presents a line plot. (H) Putative inhibitory neurons in L2/3 during the acute 0–2 weeks of implantation are entrained to both slow 2–7.5 Hz oscillations and 60–90 Hz oscillations, phase-locked to the trough of these slow (I) and fast (J) oscillations. The red bar indicates non-overlapping 95% confidence intervals between visual evoked responses and resting state at each time point, determined using a linear mixed-effects model with likelihood ratio test. The # symbol in 2 C indicates significant differences over time determined by One-way ANOVA with Tukey post hoc tests. The * symbol indicates significant differences between phase angular distribution in either the resultant mean angles (Watson–Williams test) or distribution variability (Kuiper test), or both.

Watson–William's test, $p < 0.05$). Visual inspection showed a shift in probability of entrained phase from ∼130° during the acute phase (0–2 weeks) to ∼160° during the chronic phase (9–16 weeks). Yet, there was no significant correlation of the phase angles with the firing rate of L2/3 putative excitatory neurons (Pearson's coefficient: 0.166, $p = 0.154$), which suggested the loss of synchronization. Together, these findings indicate that putative excitatory neurons in layer 2/3 progressively lose the ability to fire consistently in phase with intralaminar LFP oscillations over time.

For putative inhibitory neurons, the analysis of spike-LFP entrainment to intralaminar LFP oscillations were only reported at the acute phase (0–2 weeks) due to a loss of detectable putative inhibitory neurons (figure 3(H)). We observed that the ability of L2/3 putative inhibitory neurons to entrain to multiple frequencies was rapidly lost after the second week following implantation. Specifically, these L2/3 putative inhibitory neurons exhibited phase locking to the trough of slow 2–7.5 Hz oscillation (mean phase: 179.19 ± 47.48°) as well as 60–90 Hz gamma oscillation (mean phase: 166.45 ± 7.22°). While inhibitory neurons are known to play a critical role in local network communication [75], the observed loss in L2/3 putative inhibitory neurons suggests an early onset of local network dysfunction near the microelectrode. Together, these results indicate the L2/3 network experiences early impairment in close proximity to the microelectrode and undergoes progressive degeneration, implying a disruption in information processing during brain activity.

3.2.3. Impaired neuronal entrainment of L5/6 to intralaminar LFP oscillation

We then investigated the network function of L5/6, which serves as the major cortical output to other cortical areas and subcortical structures [76]. Analyzing the PAC of L5/6 intralaminar LFP oscillations, we found that the phase of ∼4 Hz theta oscillations strongly modulated the amplitude of 70–90 Hz gamma oscillations during visual evoked responses (figure 4(A)). The significant increase in the MI value of L5/6 theta-gamma PAC during visual evoked responses compared to the resting state (figure 4(B), linear mixed model, $p = 2.98 * 10\text{^}(-11)$) indicates the functional activation of the L5/6 intralaminar network near the microelectrode. Interestingly, the pattern of visual evoked MI over time in L5/6 resembled that of L2/3. The significantly elevated MI during visual evoked responses dropped to the level of resting state at week 8 but significantly increased again since week 14 post implantation (figure 4(B)). This suggests that the microelectrode implantation simultaneously influenced the activity of both the upstream L2/3 network and the downstream L5/6 intralaminar network.

However, the firing rate of both putative excitatory and inhibitory neuron subtypes in L5/6 remained stable over time. Both putative excitatory neurons (figure 4(C), linear mixed effect model with likelihood ratio test, $p = 0.043$) and inhibitory neurons (figure 4(D), linear mixed effect model with likelihood ratio test, $p = 0.0027$) in L5/6 exhibited a significant increase in firing rate during visual evoked responses compared to the resting state. Additionally, there were no significant differences in the firing rate of each putative neuron subtype across different time points. It is worth noting that there was sufficient detection of putative inhibitory neurons in L5/6, likely due to the increased density of inhibitory neurons distributed in the deeper cortical layers [66, 77].

Although the overall firing rates of L5/6 putative neuron subtypes remained stable over chronic implantation, it is possible that they were unable to phase-lock to the intralaminar LFP oscillatory input. Therefore, we examined the spike entrainment of L5/6 neurons to intralaminar LFP oscillation at different implantation stages. For L5/6 putative excitatory neurons, we found that 19.2% were entraining to intralaminar 2–7.5 Hz LFP oscillations, and nearly 50% were entraining to intralaminar 60–90 Hz gamma oscillation (figure 4(E)). These putative excitatory neurons in L5/6 exhibited phase-locking to the trough of the intralaminar 2–7.5 Hz oscillation during the acute 0–2 weeks, which significantly shifted in counter-clockwise direction at early chronic 3–8 weeks and chronic 9–16 weeks (figure 4(F), Watson–William's test, $p < 0.05$; Kuiper test, $p < 0.05$). Over time, there was an increase in the probability of preferred phase of ∼160 degree at early chronic 3–8 weeks stage (−158.78° ± 4.83°), followed by a decrease in the probability of preferred phase of ∼200 degree at chronic 9–16 weeks (−160.21° ± 3.90°). Additionally, the L5/6 putative excitatory neurons entraining to intralaminar 60–90 Hz high frequency oscillation were phase-locked near 140° in first 2 weeks (141.57° ± 2.59°). The mean of preferred phases significantly shifted counterclock-wise (figure 4(G), Watson–William's test, $p < 0.05$) to 146.27° ± 4.29° in early chronic 3–8 weeks and 149.44° ± 3.85° chronic 9–16 weeks. Overall, these L5/6 putative excitatory neuron altered their activity to intralaminar LFP oscillatory input during the chronic implantation period.

Meanwhile, nearly 40% of L5/6 putative inhibitory neurons were entraining to 2–7.5 Hz oscillation, and 26% were entraining to 60–90 Hz gamma oscillation (figure 4(H)). These putative inhibitory neurons in L5/6 were preferentially phase-locked to the trough of 2–7.5 Hz LFP oscillation during the acute 0–2 weeks (−172.98° ± 4.75°). However, the mean preferred phase of this entrainment was significantly shifted counterclockwise with a reduction in the probability of preferred phase in the range of ∼150°–170° (figure 4(I)).

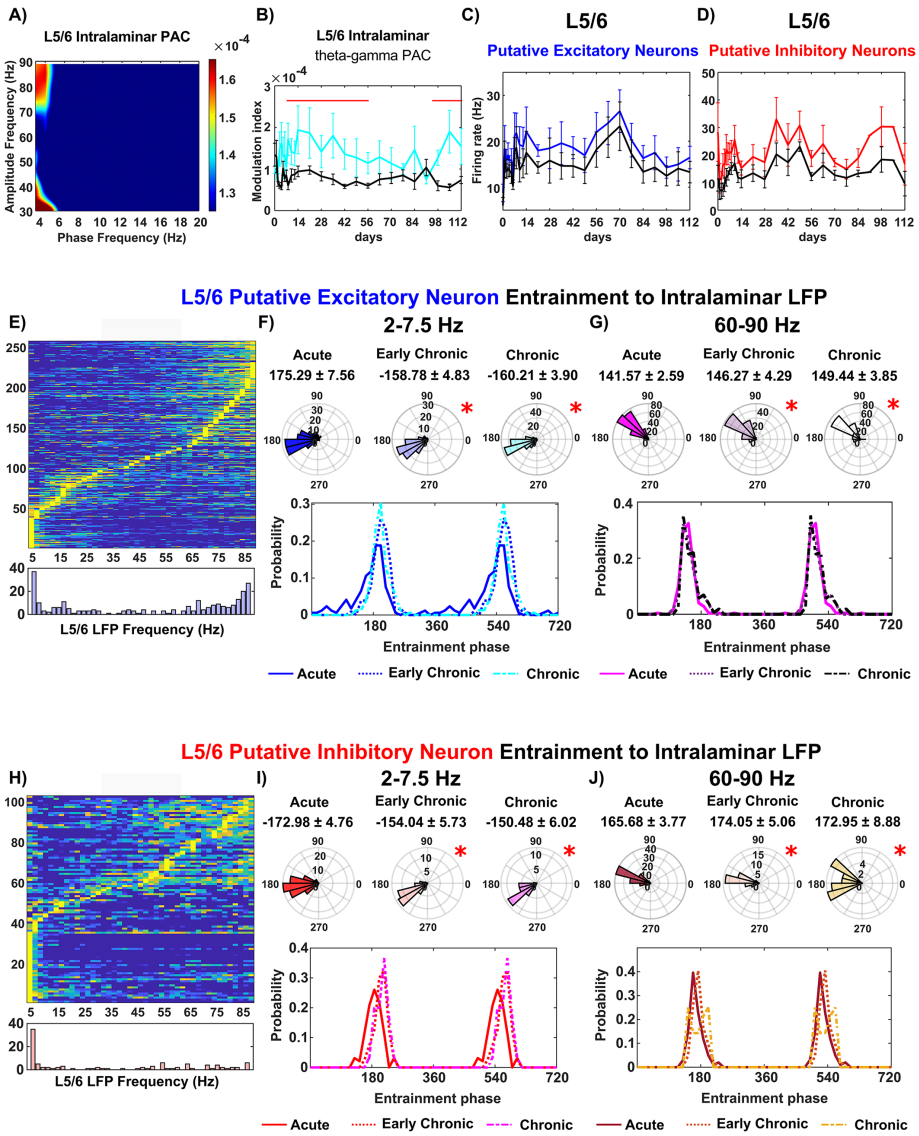

Figure 4. Impaired intralaminar connectivity near the chronically implanted microelectrode in cortical output layer L5/6. (A) Comodulogram of L5/6 intralaminar theta–gamma modulation index (MI) showing a strong phase-amplitude coupling between ∼4 Hz phase and the ∼70–90 Hz amplitude during visual evoked responses. (B) Plot demonstrating the robust modulation index (MI) between visual evoked responses (cyan) and resting state (black) over time (Linear mixed effect model with likelihood ratio test, $p = 2.98 * 10\wedge(-11)$). (C) Firing rate of putative excitatory neurons in L5/6 was significantly higher during visual evoked responses compared to the resting state (Linear mixed effect model with likelihood ratio test, $p = 0.043$). (D) Firing rate of putative inhibitory neurons in L5/6 was significantly higher during visual evoked responses compared to the resting state (Linear mixed effect model with likelihood ratio test, $p = 0.0027$). (E) Putative excitatory neurons in L5/6 were entrained to intralaminar LFP oscillations. The top panel shows normalized spike-LFP entrainment MI across frequencies for each putative excitatory neuron in L5/6 with a Rayleigh test p-value < 0.05. The bottom panel presents a summary histogram indicating that a subpopulation of putative excitatory neurons in L5/6 was entrained to intralaminar slow 2–7.5 Hz oscillations, while another subpopulation was entrained to 60–90 Hz oscillations. (F) Preferred phase distribution of putative excitatory neurons in L5/6 entraining to 2–7.5 Hz oscillations over different implantation stages (acute vs early chronic: Watson–William's test, $p = 2.27 * 10\wedge(-7)$; Kuiper test, $p < 0.001$; acute vs chronic: Watson–William's test, $p = 1.23 * 10\wedge(-8)$; Kuiper test, $p < 0.001$). The top panel shows a polar histogram, and the bottom panel presents a line plot. (G) Preferred phase distribution of putative excitatory neurons in L5/6 entraining to 60–90 Hz oscillations over different implantation stages (acute vs early chronic: Watson–William's test, $p = 0.048$; Kuiper test, $p > 0.1$; acute vs chronic: Watson–William's test, $p = 3.49 * 10\wedge(-4)$; Kuiper test, $0.05 < p < 0.1$). The top panel shows a polar histogram, and the bottom panel presents a line plot. (H) Putative inhibitory neurons in L5/6 were entrained to two frequencies of intralaminar LFP oscillations: one cluster of 2–7.5 Hz frequencies and another cluster of 60–90 Hz frequencies. (I) Preferred phase distribution of putative inhibitory neurons in L5/6 entraining to 2–7.5 Hz oscillations over different implantation stages (acute vs early chronic: Watson–William's test, $p = 5.00 * 10\wedge(-6)$; Kuiper test, $p < 0.001$; acute vs chronic: Watson–William's test, $p = 1.19 * 10\wedge(-6)$; Kuiper test, $p < 0.005$). (J) Preferred phase distribution of putative inhibitory neurons in L5/6 entraining to 60–90 Hz oscillations over different implantation stages (acute vs early chronic: Watson–William's test, $p = 0.012$; Kuiper test, $p > 0.1$; early chronic vs chronic: Watson–William's test, $p = 0.812$; Kuiper test, $p < 0.05$; acute vs chronic: Watson–William's test, $p = 0.085$; Kuiper test, $p < 0.005$). The top panel shows a polar histogram, and the bottom panel presents a line plot. The red bar indicates non-overlapping 95% confidence intervals between visual evoked responses and resting state at each time point, determined using a linear mixed-effects model with likelihood ratio test. The * symbol indicates significant differences between phase angular distribution in either the resultant mean angles (Watson–Williams test) or distribution variability (Kuiper test), or both.

Moreover, the variability of the preferred entrainment phase became significantly narrower (Watson–William's test, $p < 0.05$) from early chronic 3–8 weeks. Additionally, when entrained to intralaminar 60–90 Hz LFP, L5/6 putative inhibitory neurons were phase-locked at 165.68° ± 3.77° in acute 0–2 weeks. However, the distribution of the preferred phase significantly increased in variability (figure 4(J), Kuiper test, $p < 0.05$) at early chronic 3–8 weeks (174.05° ± 5.06°) and chronic 9–16 weeks (172.95° ± 8.88°). Overall, these L5/6 putative inhibitory neurons showed less ability to fire at a consistent phase of intralaminar LFP oscillatory activity during the chronic implantation period. Although the firing rates of detected spikes were stable, the deficits in spike-LFP entrainment and LFP cross-frequency synchronization demonstrate the dysfunctions of the L5/6 intralaminar network near the microelectrode over time.

3.3. Imbalance of cortical interlaminar connectivity near the chronically implanted electrode

3.3.1. Direction-dependent impairment in L4—L2/3 interlaminar connectivity

The chronic implantation injury had been observed to alter the functionality of the intralaminar network in a depth-dependent manner. To further understand the impact of the injury on interlaminar functional connectivity between distinct laminar structures, we first focused on L4, the input cortical layer for visual information from the thalamus, and L2/3, the subsequent processing layer [74, 78]. While our previous findings showed early impairment in the superficial L2/3 with L4 remaining a stable excitatory network over chronic implantation, we now aimed to investigate the changes in functional connectivity between L4 and L2/3.

We first determined the functional connectivity between L4 and L2/3 by analyzing the PAC of theta phase in L4 and gamma amplitude in L2/3. The MI heatmap revealed a reliable PAC relationship between ∼5 Hz phase in L4 and 60–90 Hz amplitude in L2/3 in response to visual stimulation (figure 5(A)). Additionally, we assessed the PAC between L4 theta phase and LFP amplitude across all cortical channels. The slow oscillations in L4 were exclusively phase-coupled to gamma frequency amplitude in the superficial layer corresponding to L2/3 (figure 5(B)), confirming the functional connectivity between L4 and L2/3 during visual stimulation. However, visual stimulation did not significantly elevate the MI value of L4 phase and L2/3 amplitude compared to the resting state at week 7–10 post-implantation (figure 5(C), linear mixed effect model with likelihood ratio test, $p = 5.55^{*}\ 10\text{^}(-16)$). This comparable MI value of L4 phase coupling with L2/3 LFP amplitude between visual stimulation and resting state indicated disrupted interlaminar connectivity near the microelectrode. The subsequent increase in MI values since week 11 post-implantation suggested a chronic remodeling of connectivity that enhanced L4-L2/3 synchronization.

Next, we examined the spike entrainment to LFP oscillations to investigate the directional changes in interlaminar functional connectivity between L2/3 and L4. Recent evidence suggests that neurons exhibit precise firing patterns when receiving organized oscillatory inputs [56, 79, 80]. While inhibitory neurons typically have shorter axons [81], pyramidal neurons, which are the major type of excitatory neurons in the cortex, possess long axons that can span across different laminar structures [82–84]. Making use of our putative subtype classifications in our study, we focused on putative excitatory neurons to examine interlaminar spike-LFP entrainment. For L2/3 putative excitatory neurons, approximately 33% exhibited preferential entrainment to 2–7.5 Hz oscillations in L4 (figure 5(D)). While the mean angles of preferred entrained phase were similar (Watson–Williams test, $p > 0.05$), the variance of the preferred phase distribution was significantly narrowed at the chronic 9–16 weeks (figure 5(E), Kuiper test <0.05). This subtle yet significant difference in phase entrainment of L2/3 spikes to L4 oscillatory input indicated changes in interlaminar functional connectivity from L4 to L2/3 near the microelectrode. In reverse direction, 57% putative excitatory neurons in L4 exhibited preferential entrainment to slow 2–20 Hz oscillations in L2/3 (figure 3(F)). However, the phase locking of L4 putative excitatory neurons to L2/3 oscillation underwent substantial changes over chronic implantation, with a significant counterclockwise shift in the mean phase by 100 degrees (figure 5(G), Watson–Williams test, $p < 0.05$). These significant changes in L4 spike entrainment to L2/3 LFP indicated impaired feedback connectivity as L4 excitatory neurons lost their ability to synchronize with L2/3 oscillations. Overall, the chronic implantation injury disrupts the direction-specific functional connectivity between L4 and L2/3, which aligns with the early damage observed in the L2/3 intralaminar network.

3.3.2. Imbalanced L2/3—L5 mutual connectivity

Although sensory information in L2/3 is typically relayed to the subsequent L5/6 output layer, there is also reciprocal projections from L5 to L2/3 [85–89]. To understand how this mutual connectivity is affected by chronic microelectrode implantation, we examined the interlaminar PAC of LFP oscillations between L2/3 and L5. The comodulogram of L2/3 theta phase revealed strong couplings with LFP amplitude at different cortical depths, including L2/3 itself, L4, and shallow L5 (figure 6(A)). The coupling between L2/3 theta phase and L5 gamma amplitude (∼55–65 Hz) during visual evoked responses was significantly higher than during resting state until week 12 post-implantation (figure 6(B),

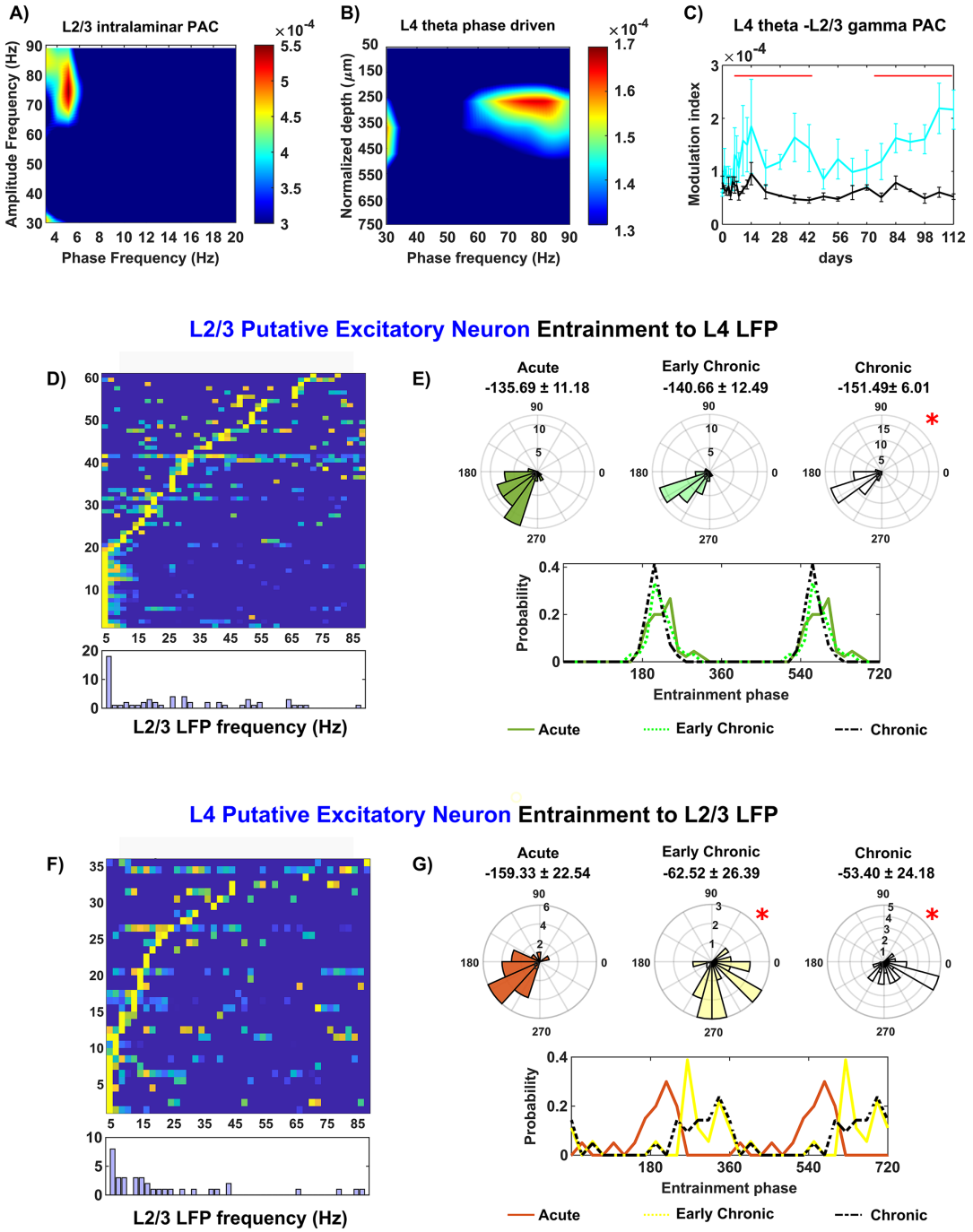

Figure 5. Impaired interlaminar connectivity between L4 and L2/3 during chronic microelectrode implantation. (A) Comodulogram displaying the phase-amplitude coupling (PAC) between slow oscillation frequency (2–20 Hz) in L4 and LFP amplitude (30–90 Hz) in L2/3 during visual stimulation. The modulation index (MI) peaked at $5.32 \pm 0.15 \times 10^{\wedge}-4$, indicating strong coupling between 5 Hz theta phase in L4 and 60–90 Hz gamma amplitude in L2/3. (B) PAC comodulogram between slow oscillation (4–7.5 Hz theta frequencies) in L4 and LFP amplitude across all cortical channels, highlighting the interlaminar coupling of L4 phase to high gamma amplitude in the superficial layer corresponding to L2/3. (C) Plot showing the MI of L4 theta phase-L2/3 gamma amplitude during visual evoked responses (cyan) and resting state (black) over time (Linear mixed effect model with likelihood ratio test, $p = 5.55 * 10^{\wedge}(-16)$). (D) Interlaminar entrainment of L2/3 putative excitatory neurons to L4 LFP oscillations. The top panel displays the normalized entrainment MI of each L2/3 putative excitatory neuron to L4 oscillations across frequencies, while the bottom panel presents a summary histogram showing that most neurons were phase entrained to 2–7.5 Hz. (E) Preferred phase distribution of L2/3 putative excitatory neurons entraining to L4 slow oscillation over different implantation stages (acute vs early chronic: Watson–William's test, $p = 0.480$; Kuiper test, $p > 0.1$; acute vs chronic: Watson–William's test, $p = 0.007$; Kuiper test, $0.05 < p < 0.1$), depicted in a polar histogram (top) and a line plot (bottom). (F) Preferential entrainment of L4 putative excitatory neurons to L2/3 slow oscillations over the 2–20 Hz frequency range. (G) Preferred phase distribution of L4 putative excitatory neurons entraining to L2/3 2–20 Hz oscillation over different implantation stages (acute vs early chronic: Watson–William's test, $p = 1.96 * 10^{\wedge}(-6)$; Kuiper test, $p < 0.001$; acute vs chronic: Watson–William's test, $p = 1.36 * 10^{\wedge}(-7)$; Kuiper test, $p < 0.001$), represented in a polar histogram (top) and a line plot (bottom). The red bar indicates non-overlapping 95% confidence intervals between visual evoked responses and resting state at each time point, determined using a linear mixed-effects model with likelihood ratio test. The * symbol indicates significant differences in phase angular distribution, either in the resultant mean angles (Watson–Williams test), distribution variability (Kuiper test), or both.

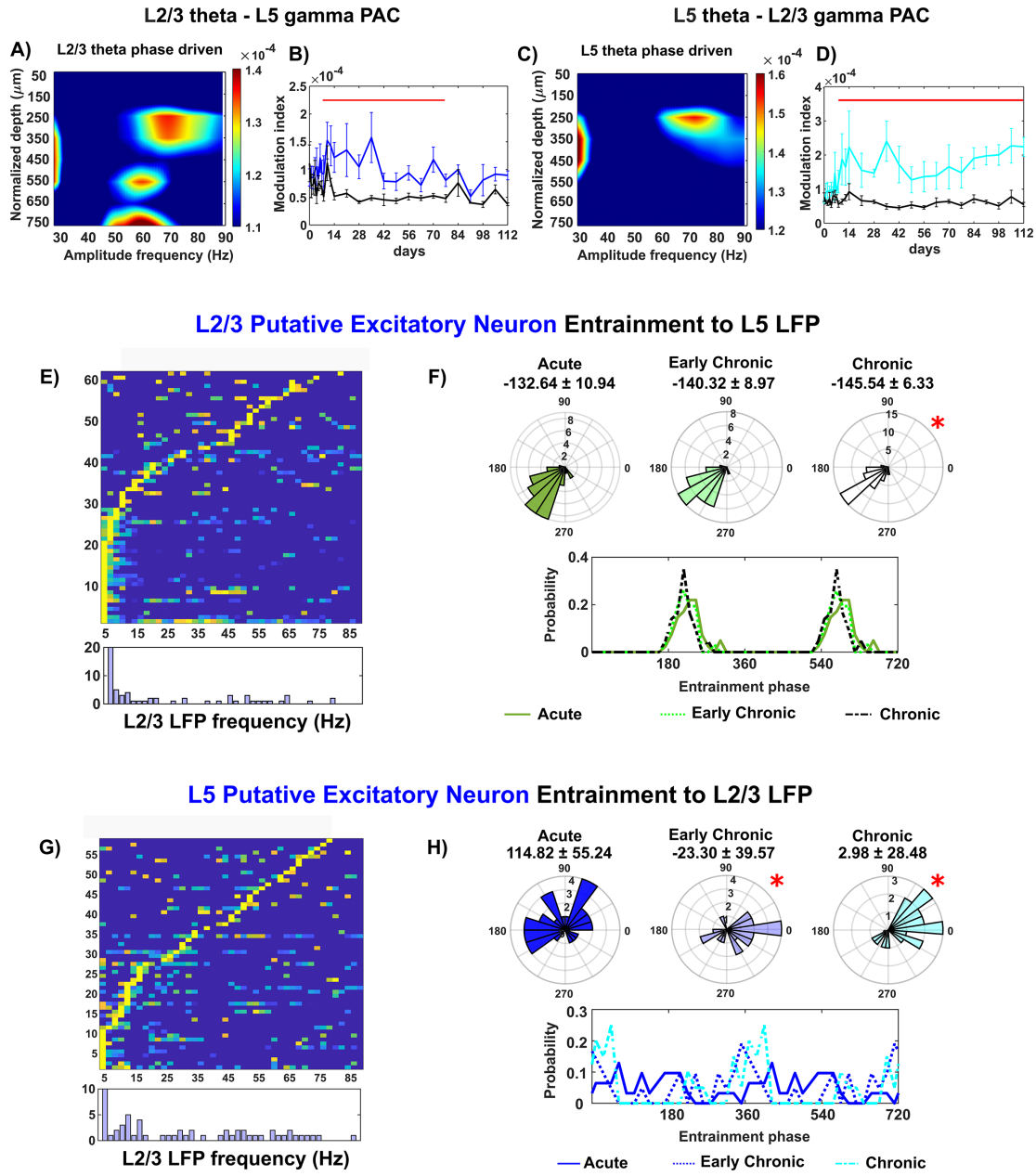

Figure 6. The impaired balance of mutual connectivity between L2/3 and L5 over chronic microelectrode implantation. (A). PAC comodulogram between L2/3 theta phases and LFP amplitude across all cortical channels. The robust MI cluster over 55–65 Hz amplitude frequency at 550 μm below surface demonstrates the L2/3-L5 connectivity. (B) The MI of L2/3 theta phase coupling to L5 gamma amplitude during visual evoke (blue) gradually decreased to the level of resting state (black) over time (Linear mixed effect model with likelihood ratio test, $p = 8.44\ ^*10\hat{}(-9)$). (C). The L5 reciprocal projection to L2/3 was represented as the robust L5 theta phase coupling to ∼60–80 Hz amplitude at 250 μm below the brain surface. (D). The MI value of this PAC during visual evoke was significantly elevated compared to resting state over the entire 16 week implantation (Linear mixed effect model with likelihood ratio test, $p = 1.37\ ^*10\hat{}(-12)$). (E). L2/3 putative excitatory neurons were preferentially entrained to L5 2–7.5 Hz oscillation. Top: normalized entrainment MI of each L2/3 putative excitatory neuron to L5 oscillations across frequencies. Bottom: summary histogram. (F). Preferred phase distribution of L2/3 putative excitatory neurons entraining to L5 slow oscillation over different implantation stages (acute vs early chronic: Watson–William's test, $p = 0.214$; Kuiper test, $p > 0.1$; acute vs chronic: Watson–William's test, $p = 0.015$; Kuiper test, $p > 0.1$) (Top: polar histogram; bottom: line plot). (G). L5 putative excitatory neurons with a Rayleigh test p value < 0.05 were preferentially entrained to 2–20 Hz oscillations in L2/3. (H). Preferred phase distribution of L5 putative excitatory neurons entraining to L2/3 2–20 Hz oscillation over different implantation stages (acute vs early chronic: Watson–William's test, $p = 3.42\ ^*10\hat{}(-6)$; Kuiper test, $p < 0.02$; acute vs chronic: Watson–William's test, $p = 2.78\ ^*10\hat{}(-5)$; Kuiper test, $p < 0.001$) (Top: polar histogram; bottom: line plot). Red bar indicates non-overlapping 95% confidence intervals between visual evoke and resting state at each time point using a linear mixed effects model with likelihood ratio test. The * indicates the significant differences between phase angular distribution in either the resultant mean angles (Watson–Williams test) or distribution variability (Kuiper test), or both.

linear mixed effect model with likelihood ratio test, $p = 8.44\ ^*\ 10\hat{}(-9)$). However, this coupling progressively declined over time, indicating a loss of L2/3's ability to synchronize L5 LFP oscillatory activity at the chronic implantation period. In the opposite direction, the L5 theta oscillation was exclusively

coupled to ∼60–80 Hz oscillation amplitude in L2/3 (figure 6(C)), indicating the reciprocal functional projection from L5 to L2/3. Interestingly, the coupling between L5 theta and L2/3 gamma during visual evoked responses was consistently higher than during resting state throughout the 16 week implantation period (figure 6(D), linear mixed effect model with likelihood ratio test, $p = 1.37\ ^{*}10(-12)$), suggesting an enhanced interlaminar connectivity from L5 to L2/3 near the microelectrode.

Spike entrainment analysis further revealed changes in the synchronization between L2/3 and L5 neurons to LFP oscillations. For L2/3 putative excitatory neurons, 38% exhibited preferential entrainment to L5 slow 2–7.5 Hz oscillation (figure 6(E)). Additionally, there was a shift in phase locking to L5 slow oscillation in a clockwise direction at the chronic implantation stage (figure 6(F), Watson–Williams test, $p < 0.05$). Visual observation demonstrated a reduced probability of ∼240° entrained phases at chronic implantation stage. Conversely, nearly 48% of putative excitatory neurons in L5 were entraining to 4–20 Hz oscillation in L2/3 (figure 6(G)). L5 putative excitatory neurons showed a substantial degradation in their synchronization to L2/3 oscillatory input, with significant changes in both mean phases and variance of preferred phase distribution over time (figure 6(H), Watson–Williams test, $p < 0.05$; Kuiper test, $p < 0.05$). These results indicate a direction-specific impairment in the interlaminar connectivity between L2/3 and L5, leading to imbalanced mutual communication during information processing in the cortex. The dysfunctions observed in L2/3 intralaminar networks likely contribute to the impaired functional projection from L2/3 to L5, while the enhanced functionality of the L5 projection back to L2/3 suggests compensatory mechanisms during chronic implantation.

3.4. Disruption of hippocampal network activity during chronic microelectrode implantation

As sensory information is relayed from cortex to hippocampus, we investigated the laminar network near the microelectrode tip in the hippocampal CA1 region. While the cortical network near the implanted microelectrode showed significant activation in response to visual stimuli, the firing rate profile in the hippocampus CA1 region exhibited limited network responses (figures 1(E) and (G)). To assess the activation of the CA1 network near the microelectrode, we compared the PAC synchronization within CA1 LFP oscillations between visual evoke and resting state conditions. Although the CA1 theta oscillation was coupled to intralaminar gamma amplitude (figures 7(A) and (B)), there was no significant difference in PAC MI between these two conditions over time (figure 7(C)). Furthermore, the firing rates of putative excitatory neurons in CA1 did not show a statistically significant difference between visual evoke and resting state throughout the 16 week implantation (figure 7(D)).

However, the entrainment analysis of CA1 putative excitatory neurons to intralaminar LFP oscillations revealed impairments in local neuron communication. Around 63% of putative excitatory neurons in CA1 exhibited preferential phase entrainment to 2–7.5 Hz slow oscillation (figure 7(E)). The phase locking behavior in the acute 0–2 weeks stage (169.58° ± 14.35°) was significantly different compared to the early chronic 3–8 weeks (148.79° ± 22.44°) and chronic 9–16 weeks (143.53° ± 20.51°) stages (figure 7(F)). The mean phase showed a significant clockwise shift (Watson–Williams test, $p < 0.05$), and the distribution of preferred phases exhibited increased variability (Kuiper test, $p < 0.05$) over time. Visual observation suggests that both early chronic and chronic implantation stages reduced the probability of preferred phases ∼180°–240° compared to the acute 0–2 weeks stage. These results indicate that the CA1 neurons adjacent to the microelectrode were less able to respond appropriately to synchronized oscillatory inputs. In summary, chronic implantation led to local impairments in the CA1 circuit, including a chronic dysfunction in individual neural response to surrounding LFP oscillations.

3.5. Histology of neuronal subtypes in different brain laminar structures near the chronic microelectrode

Given electrophysiological changes in functional network connectivity over time, we assessed the integrity of neuronal populations following 16 week chronic implantation by immunohistology. Immunohistochemical staining markers were used to label different neuronal subtypes (CaMKIIα for excitatory neurons and GAD67 for inhibitory neurons) and dendrites labeled by MAP2. Coronal sections of the tissue were examined to visualize the depth distribution of these markers in the cortex and hippocampus CA1.

In the cortex, a reduction in fluorescence intensity of CaMKIIα (figure 8(A)) and GAD67 (figure 8(B)) was observed near the implant site, particularly in the superficial cortical layers. This loss indicated damage to both excitatory and inhibitory neurons in the superficial cortical depth. Additionally, a significant decrease in MAP2 fluorescence was observed at superficial depths (figure 8(C)), suggesting impaired dendritic structure in the superficial network due to the implantation injury. These histological findings corresponded with the electrophysiological measurements showing impairment in the superficial L2/3 region of the cortex.

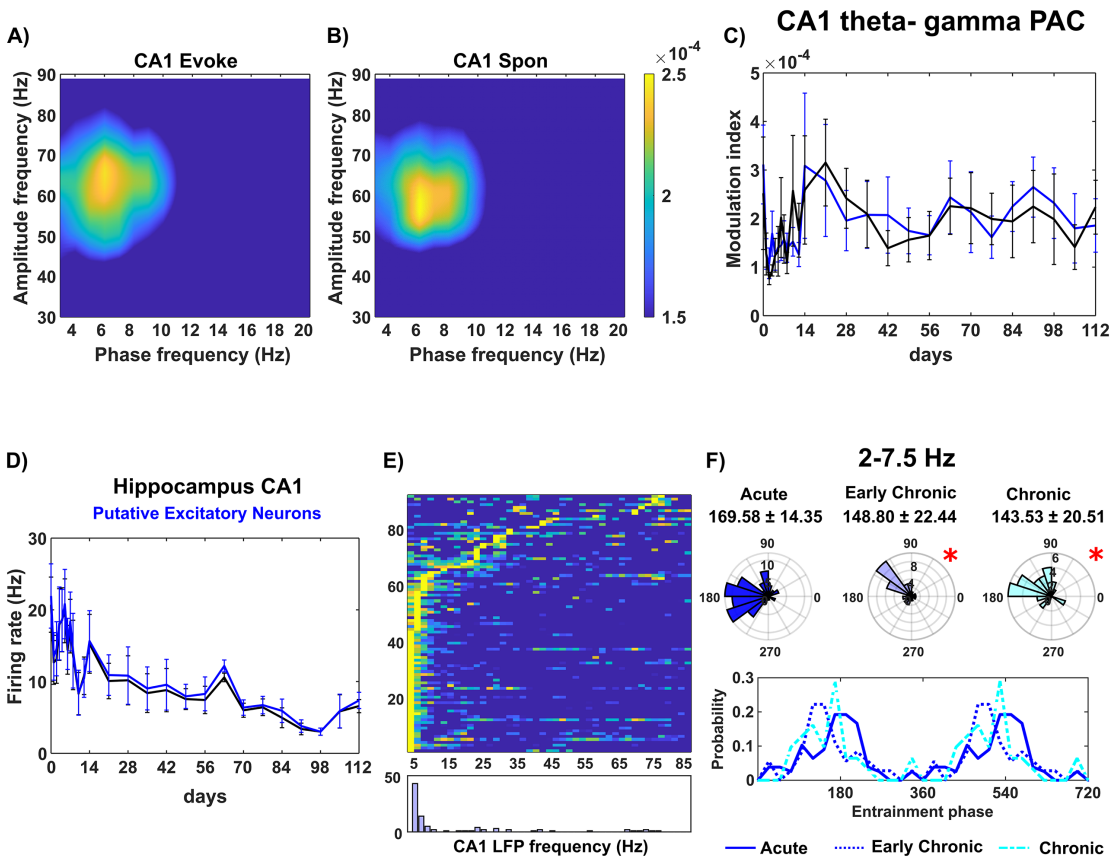

Figure 7. Disruption of hippocampus CA1 communication over chronic implantation. PAC comodulogram of CA1 LFP oscillation between slow frequency (2–20 Hz) phases and high-frequency (30–90 Hz) amplitudes during visual evoke (A) and resting state (B). Robust MI coupling was observed between ∼4–8 Hz phases and 50–70 Hz amplitude in both conditions. (C). The MI of CA1 theta–gamma PAC during visual evoke (cyan) was comparable to that during resting state (black) over time (Linear mixed effect model with likelihood ratio test, $p = 0.927$). (D). Firing rates of putative excitatory neurons in CA1 during visual evoke (blue) and resting state (black) over time (Linear mixed effect model with likelihood ratio test, $p = 0.961$). (E). The majority of CA1 putative excitatory neurons exhibited preferential entrainment to CA1 2–7.5 Hz oscillation. Top: normalized entrainment MI of each CA1 putative excitatory neuron to intralaminar LFP oscillations across frequencies. Bottom: Summary histogram. (F). Preferred phase distribution of CA1 putative excitatory neurons entraining to 2–7.5 Hz oscillation across different implantation stages (acute vs early chronic: Watson–William's test, $p = 0.104$; Kuiper test, $p < 0.02$; acute vs chronic: Watson–William's test, $p = 0.039$; Kuiper test, $p > 0.1$) (Top: polar histogram; Bottom: line plot). Asterisks(*) Indicates significant differences in phase angular distribution, including resultant mean angles (Watson–Williams test) and distribution variability (Kuiper test), or both.

In the hippocampal CA1 region, dense CaMKIIα+ Nissl+ soma showed reduced fluorescence intensity adjacent to the implant (figure 8(D)), indicating the impairment of CA1 pyramidal neurons located in the SP. Few GAD67+ Nissl+ cells were observed in the hippocampal CA1 region, making it difficult to assess inhibitory network integrity in this area (figure 8(E)). Interestingly, low levels of MAP2 fluorescence were observed in the region beneath the CA1 soma layer (figure 8(F), yellow arrow), corresponding to the CA1 stratum radiatum (SR) where dendrites input to pyramidal cells in the SP. This finding suggested that chronic microelectrode implantation impaired the appropriate synaptic inputs to pyramidal neurons. Overall, these histological observations supported the electrophysiological results, demonstrating depth-dependent tissue changes caused by chronic microelectrode implantation.

4. Discussion

Intracortical microelectrodes have demonstrated potential as a therapeutic tool for neurological disorders [3, 4, 10, 13, 17]. However, the gradual decline in recording quality during long-term implantation leads to the instability of BCI decoders over time creating a major challenge in their clinical application [9, 14, 24, 90]. BCI decoders are algorithms that translate brain signals into digital commands for computer and robotic outputs [91]. However, the brain signals generated by the neural networks are subject to changes produced by tissue degeneration such as neuronal density loss and glial encapsulation near the implant site [28]. The instability of brain signals can degrade BCI performance, requiring frequent recalibration of the BCI decoders [13, 92, 93], a time- and effort-consuming process

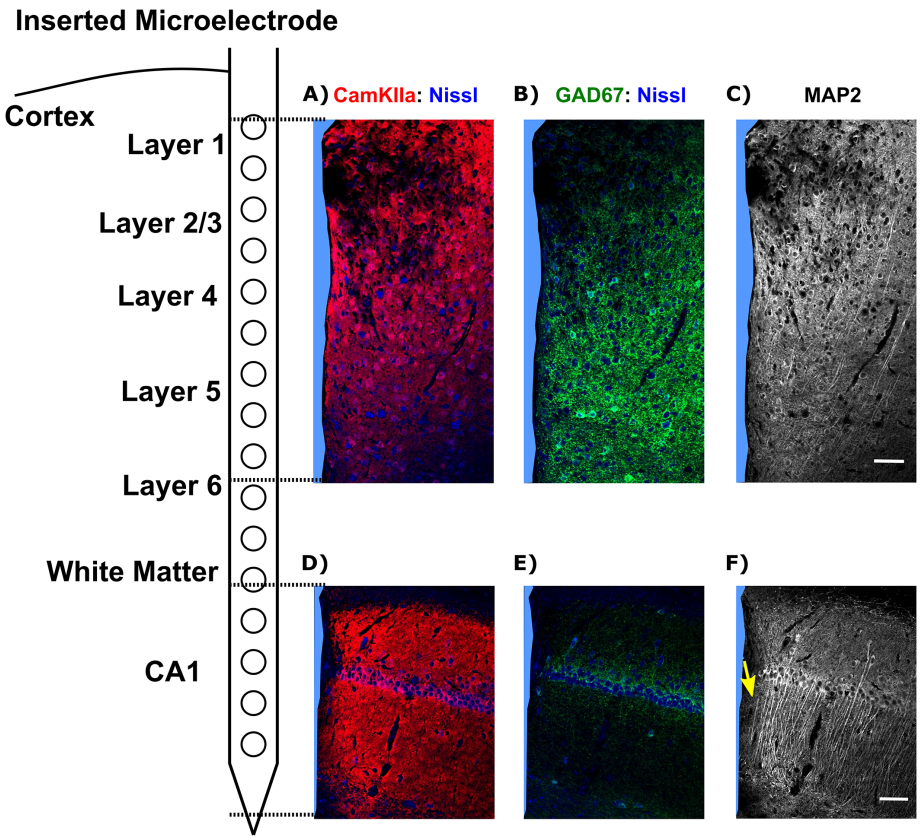

Figure 8. Histological evaluation reveals prominent loss of neural markers at superficial cortical depth relative to deep structures. Representative histological images demonstrated loss of CaMKIIα+ Nissl+ excitatory neurons (A), GAD67+ Nissl+ inhibitory neurons (B), and MAP2+ dendrites (C) near the microelectrode at superficial cortical depths. Images of the hippocampus CA1 showed the distribution of CaMKIIα+ Nissl+ excitatory neurons (D), GAD67+ Nissl+ inhibitory neurons (E), and MAP2+ dendrites (F) near the chronically implanted microelectrode. Microelectrode shanks are labeled in blue. Scale bar = 50 μm.

that causes substantial inconvenience to the patients during each session.

To facilitate addressing these challenges, this study aims to examine how functional network connectivity near the implanted microelectrode changes over time. Our findings revealed a depth-dependent degradation in intralaminar functional connectivity. The superficial layers (L2/3) showed early impairment with a loss of putative inhibitory neuron detection and a significant decrease in the firing rate of putative excitatory neurons. Interlaminar functional connectivity changes near the implant were found to be directional, specifically between L2/3 and L5. In the hippocampal CA1 region near the implant there were changes in the precise timing of spikes in response to oscillatory LFP activity. These findings provide valuable insights into the changes in functional network connectivity due to tissue reactions near the chronically implanted microelectrode, separate from neuroplasticity changes linked to learning. Elucidating the mechanisms behind the decline in signal quality over time can contribute to the design of therapeutic strategies for improving the tissue health near the chronically implanted electrode. Additionally, this knowledge can inform the development of more stable and reliable BCI decoders.

4.1. Changes to excitatory activity may contribute to dysfunctions in laminar network connectivity near the chronically implanted microelectrode

The majority of cortical neurons are excitatory glutamatergic neurons, interconnected within and across layers to facilitate recurrent excitation in brain circuits [94]. This local recurrent excitation could implement amplification and thus elevate network connectivity [95]. However, networks with high amplification are sensitive to disruption, since the loss of even a few neurons involved in recurrent excitation can impair information processing in the L2/3 network [94]. Our findings reveal a layer-dependent profile of putative excitatory neuron firing rates which decreased significantly in L2/3 during the chronic implantation period (figure 3(D)). This observation suggests a disruption in recurrent excitation within the L2/3 local network, which may affect L2/3 network connectivity. Additionally, L2/3 putative excitatory neurons exhibit improper entrainment to intralaminar LFP oscillatory input (figures 3(E)–(G)) during the chronic implantation period, providing evidence of dysfunction in excitatory activity in the L2/3 intralaminar network. The recurrent network of excitatory neurons in L2/3 plays a vital role in sensory processing including feature extraction,

specific input amplification, and information integration across different sensory modalities [83, 94, 96]. Therefore, impairment to L2/3 excitatory activity near the chronically implanted microelectrode could result in network functionality deficits, potentially affecting the quality and reliability of signals received from the implant for further BCI applications.

Moreover, L2/3 serves as a crucial relay station for ascending and descending projections, mediating communication between superficial and deep cortical layers [83]. Recurrent excitation exists between L2/3 and L5 as L2/3 pyramidal neurons play a vital role in amplifying sensory-evoked responses in L5 neurons [78]. Therefore, the impairment of L2/3 excitatory activity may affect its interlaminar excitatory projection to L5, which could explain the substantial degradation of L5 putative excitatory neuron synchronization to L2/3 oscillatory input (figures 6(G) and (H)). Furthermore, the excitatory activity within the L5/6 intralaminar network is influenced, as suggested by the changes in responsiveness of the L5/6 putative excitatory neurons to intralaminar LFP oscillatory activity over time (figures 4(E)–(G)). Thus, disruption in the excitatory activity of L2/3 may be associated with the disturbances in the deeper layers that serve as cortical outputs near the chronically implanted microelectrode. However, further studies are necessary to ascertain whether the changes in L5/6 putative excitatory neuron activity result from a cascading impact originating from L2/3 disruptions, or whether they are directly influenced by chronic implantation injury. Potential future investigations could focus on unraveling the sequence of these changes to deepen our understanding of chronic alterations in cortical networks near the implanted microelectrode. One possible approach could involve confining the microelectrode implantation to L2/3 and scrutinizing excitatory activity through the assessment of glutamate synaptic density and postsynaptic calcium dynamics in the deep layers L5/6. This evaluation may help examine whether there is a cascade effect from L2/3 to L5/6 when the microelectrode does not cause injury in the deep layers.

In addition to cortical networks, the hippocampus CA1 region also experiences a shift in the entrainment of putative excitatory neurons to LFP oscillatory input (figure 7), suggesting a disruption in appropriate excitatory synaptic connectivity in CA1 near the implanted microelectrode. The stiff microelectrode implantation is known to cause more concentrated mechanical strain in the deeper tissue near the tip, as compared to the superficial layers [25]. In this study, microelectrodes were perpendicularly inserted 1600 μm below the brain surface, positioning the tip near the CA1. Thus, brain tissue in CA1 near the tip is likely to experience increased mechanical strain, potentially triggering microglial mechanosensory response and leading more microglial cells to transform to an activated state [97]. Implantation-induced inflammation has been associated with the activation of Toll-like receptor (TLR) 2 and TLR4 in microglia, which can reduce long-term potentiation [98]. This could be a potential pathway leading to the observed disruption of putative excitatory neurons' response to LFP synaptic input in CA1 (figure 7(F)). However, the comprehensive mechanisms through which inflammation impacts synaptic functionality in the neural circuits near the implanted microelectrode remain to be fully elucidated and warrant further research.

4.2. Changes to inhibitory activity may contribute to dysfunctions in laminar network connectivity near the chronically implanted microelectrode

Although representing only a small fraction of the total neuronal population, inhibitory neurons play a critical role within neural networks [66, 99]. Inhibitory neuron activity helps to balance excitation in the network, and this balance is essential for proper information processing in the brain [75, 100]. Feedback inhibition is a common activity motif at the network level, involving a set of excitatory neurons stimulating inhibitory neurons, which in turn suppress the activity of the same population of excitatory cells [101, 102]. This feedback inhibition is vital for synchronization of populational firing of excitatory neurons [101]. In this study, we noted a decline in the involvement of L2/3 putative inhibitory neurons in visually evoked activation near the implanted microelectrode (figure 3(C)), suggesting an early impairment of L2/3 intralaminar feedback inhibition. Additionally, alterations in L2/3 intralaminar spike entrainment to LFP (figures 3(E)–(J)), along with decreased firing rates of putative excitatory neurons (figure 3(D)), indicate a loss of synchronized excitatory activity. These observations collectively suggest a disruption in the excitation-inhibition balance in the L2/3 near the microelectrode, which may influence accurate information processing. However, additional research is needed to investigate whether these modifications in L2/3 inhibitory neuronal activity are the driving force behind changes in excitatory responses to chronic implantation injury.

Moreover, impairment in inhibitory activity could potentially disrupt interlaminar communication with deeper layers. Feed-forward inhibition typically occurs between different cortical layers, where excitatory neurons stimulate intralaminar inhibitory cells that subsequently inhibit a group of postsynaptic excitatory neurons in another layer [101, 103]. Thus, feed-forward inhibition is critical for maintaining interlaminar network connectivity [101, 103]. Our observations indicate a loss of functional network connectivity from L2/3 to L5 (figures 6(A) and (B)) and from L2/3 to L4 (figures 5(F) and (G)), along with the loss detection of L2/3 putative inhibitory

neurons (figure 3). These findings suggest that the impairment of inhibitory activity in L2/3 may lead to deficits in feed-forward inhibition to the deeper layers, explaining the decreased interlaminar network connectivity with L2/3 in the descending direction. Furthermore, it is likely that diminished inhibitory input from L2/3 affects the balance of excitation and inhibition within the L5 intralaminar network, subsequently contributing to alterations in synchronization from L5 to L2/3. Interestingly, we noted that the connectivity in the reverse ascending direction, from L4 to L2/3 (figure 5(C)) and L5 to L2/3 (figures 6(C) and (D)), is heightened. This heightened interlaminar connectivity from L5 to L2/3 could potentially indicate abnormal amplification from L5 due to a loss of L2/3 feed-forward inhibition. An imbalance in the reciprocal connectivity between L2/3 and L5 could thus alter network dynamics and result in modifications to neuronal entrainments to LFP oscillatory input. Future studies are required to determine if, and how, the impairments in inhibitory activity in L2/3 directly contribute to the observed changes in the interlaminar connectivity with deeper layers. Additionally, the specific impact of these changes on the excitation-inhibition balance within L5 intralaminar network and on network dynamics should be explored.

4.3. Changes in metabolic activity may contribute to alterations in laminar network connectivity near the microelectrode

Deficiencies in metabolic supply to neurons can lead to dysfunctions within neural networks, which may be associated with the selective functional impairments observed in putative inhibitory neurons within the superficial layer L2/3. Firstly, the reduced detection of putative inhibitory neurons at L2/3 is likely associated with the lower density of interneurons at superficial layers compared to the deeper layers [104]. Additionally, compared to excitatory neurons, the activation of inhibitory interneurons that have higher levels of cytochrome c oxidase and an increased number of mitochondria demands substantial energy consumption [104]. However, the insertion of a microelectrode also disrupts blood vessels, resulting in a localized loss of perfusion and metabolites to brain tissue [28]. Although the insertion of microelectrode avoided the major surface blood vessels, it is inevitable that the position of large-dimension silicon shank was in close proximity to large blood vessels at superficial depth. It has been established that the tissue response is more severe when the probe is implanted near large blood vessels (>5 μm diameter) as compared to a region with small vessels [32]. Thus, the probe at deeper brain structures with small capillaries might experience less tissue injury compared to superficial layers. Additionally, the stress and strain introduced by microelectrode implantation concentrated at the superficial cortical depth, which can damage vessel integrity and subsequentially disturb the blood flow and reduce the vessel permeability [105–107]. Moreover, astrocytes [35, 108, 109] and oligodendrocytes [41, 43] that mediate local delivery of metabolites to neurons undergo more structural changes in response to implantation injury at superficial layers [110, 111], which may further compromise the metabolic supply for neural network functionality near the microelectrode. Therefore, this disruption to vascular integrity and glial reactivity potentially reduces the availability of glucose and oxygen for neuronal activity and against inflammation injury [28, 31, 40], which may explain the early detection loss of metabolically intensive inhibitory neurons.

Inefficient waste removal may contribute to changes in laminar network connectivity near the chronically implanted microelectrode. A buildup of toxic substances to neurons resulting from neuroinflammation following electrode implantation may be associated with the progressive degeneration of L2/3 network functionality (figure 3). While microglia with phagocytic capacity quickly become activated in response to microelectrode implantation, there is a mismatch between this immediate microglial activity and the subsequent neuron loss near the microelectrode [112–116]. Microglial phagocytic repair might not effectively remove the cell debris, leading to sustained neuroinflammation, particularly in the superficial layers. Future studies could explore the impacts of implantation on microglial phagocytosis and how these might influence the functionality of the implanted microelectrode.

4.4. Network instability and decoder performance: decoupling plastic learning and network degeneration in disease and injury

The stability of BCI decoders, which convert brain signals into digital information, is crucial for their effective performance, particularly in long-term applications like neuroprosthetics and clinical treatments. However, the long-term decoder performance is hindered by the neural reorganization produced by implantation-induced injury and/or 'plasticity' [13, 92, 93]. Therefore, gaining a comprehensive understanding of changes in neural network activity can assist in designing decoders with machine learning algorithms that can adapt to shifting neural data and maintain their performance over time. BCI technology typically employs Utah arrays approved for clinical use [12, 17, 37, 117]. The tissue changes around these implanted arrays significantly influence BCI decoder stability over the implantation period [118, 119]. The frequent need to retrain BCI decoders, sometimes within hours or days, suggests a dynamic tissue change affecting the neural circuitry near the implanted Utah arrays. The implantation of Utah arrays induces brain trauma, resulting in neuropathological changes similar to those seen

with single-shank microelectrodes, including acute neuroinflammation and a chronic FBR [119–121].

The immediate instability of BCI decoders following implantation (hours to days post-implantation) could be associated with various factors such as microglia activation, astrocyte reactivity, decreased blood flow, and disturbances in spine plasticity. The insertion of the rigid Utah arrays triggers glial cells' response [122], potentially disrupting the critical balance between neuronal excitation and inhibition [123]. This disturbance, alongside reduced blood flow and the vulnerability of neuronal dendritic spines to inflammation, can disrupt network connectivity shortly after implantation. The insertion of stiff Utah arrays triggers activation of microglia and astrocytes. These glial cells move their processes toward the probe, migrate their soma to the implantation site, and form an encapsulating layer [35, 116]. Microglia play a crucial role in modulating neuronal network activity by preventing hyperexcitability [124, 125], while astrocytes modulate inhibitory activity through the secretion of GABA gliotransmitters [126, 127]. Thus, changes in microglial and astrocytic activity due to probe implantation likely disrupt the excitation-inhibition balance during the acute phase. The reduced blood flow, similar to what is observed with single-shank microelectrodes, could compromise energy availability for network activation, leading to unstable network activity [31]. Moreover, neuronal dendritic spines, essential for network connectivity, are highly vulnerable to the high gradient of pro-inflammatory cytokines and chemokines [128, 129], which could be resulted from activated microglia and astrocytes near the implanted probe. Therefore, implantation injury affects the dynamics of spine formation, elimination, and stabilization, causing disruptions in network connectivity shortly after implantation.

During the early chronic phase, decoder instability may also be linked to oligodendrocyte degeneration and demyelination. Oligodendrocytes have myelin processes with a large contact area to axons, providing electrical modulation and metabolic support for neuronal network functionality [130, 131]. However, these cells are vulnerable to inflammatory environments and undergo progressive myelin degradation near the single-shank microelectrode [41]. Damage to oligodendrocytes and myelin in the local network has been linked to signal transmission failure, including impaired firing rates, rapid signal fatigue, and reduced sustainability of neuronal firing [42, 132–134]. Therefore, the significant reduction in firing rate of putative excitatory neurons by week 12 and the loss of network activation between weeks 9 and 11 in this study, which used a single-shank microelectrode, are likely related to oligodendrocyte impairment in superficial layers. Thus, BCI decoder instability during the early chronic phase of Utah array implantation could be tied to the loss of nearby oligodendrocytes and demyelination. Our findings, which show a significant reduction in the firing rate of putative excitatory neurons and network activation with single-shank microelectrodes, suggest a similar impact could occur with Utah array implantation. Furthermore, chronic instability in BCI decoder performance could be related to neuronal degeneration and death. A phenomenon observed across various species [40, 119, 135]. Our observations from the histological analysis of the neuronal population 16 weeks after single-shank microelectrode implantation show a reduction in neuronal population near the microelectrode at superficial depths (supplementary figure 3). Given that the Utah array is larger than the single-shank microelectrode [37], the tissue injury caused by the Utah array is likely to be more severe and result in greater impairment in intra- and inter-laminar network functionality. Together, these discussed possibilities indicate how implantation injury might disturb tissue environment and network functionality that contribute to BCI decoder instability. However, future research is essential to more directly elucidate the interplay between biological responses to implantation and BCI decoder performance across different stages of implantation.

4.5. Limitations

There are several limitations in this study. First, the classification of putative neuronal subtypes based on spike width has some constraints. While this approach is commonly used in many studies to separate sorted waveforms into different functional groups [55, 60], it is important to note that further validation is required to confirm the physiological identification of these neuronal subtypes [136]. Optogenetic strategies, combined with electrophysiological measurements, could be applied to validate the identification of neurons classified based on spike width. Alternatively, other parameters such as firing rates, depth location, and monosynaptic connections through short-latency spike cross-correlograms could be used to further cluster functional subtypes of sorted SU waveforms. Moreover, additional immunohistological quantifications would be helpful to understand the longitudinal impact of implantation injury on different brain laminar structures. While CaMKII*a* is widely used for labeling excitatory neurons, multiple types of GABAergic interneruons are also labeled by the viral expression driven by CaMKII*a* promotor [137]. Therefore, markers such as VGLUT could be included to determine the population of excitatory neurons near the implanted microelectrode. However, it should be acknowledged that despite the limitations, our results still provide insights into different neuronal subtypes with distinct electrophysiological features in response to chronic implantation injury.

Secondly, we utilized cross-frequency coupling (PAC) and spike-LFP coupling to investigate functional connectivity within and across different laminar structures. However, whether the changes in functional connectivity involve changes in anatomical network connections in response to microelectrode implantation over chronic time scales remain unknown. While electrophysiological measures provide insights into synaptic and firing activity near the implant, further investigation through anatomical evaluation, such as immunohistochemical staining of presynaptic markers (e.g. Neurexin-3α, SNAP-25, Synapsin) and postsynaptic markers (e.g. Gephyrin, Homer1, Synapse-Associated Protein-102), can provide direct evidence on how synaptic connectivity plasticity is affected near the implant in various laminar structures. These experiments will help bridge the gap between circuit functionality and tissue reactions, providing a deeper understanding of the underlying mechanisms.

A third limitation inherently arises from the sampling of the electrophysiological activity from a random set of neurons surrounding the microelectrode. The limits of a recording site allow for the detection of only about 5 SUs [138], yet the neuronal density near the implant is about to 1500 cells mm^{-2} at 50–100 μm [40]. Thus, it becomes challenging to track the same population of neurons over time. Therefore, future studies should consider incorporating in vivo imaging techniques that can reveal the real-time dynamics of neuronal activity. These imaging methods can be performed in parallel with electrophysiological recording during visual stimulation, allowing for a comprehensive assessment of network functionality over chronic time periods. This integrated approach would provide valuable insights into the spatial and temporal characteristics of neuronal activity in response to implantation injury, further enhancing our understanding of the underlying mechanisms and dynamics within the neural circuitry.

Fourth, our observations regarding CA1 activity in response to visual stimulation (figure 7) indicate that the CA1 circuit near the implanted microelectrodes in this study was not strongly activated during drifting bar visual stimulation. Hippocampus is highly involved in processing visual scenes for discrimination and memory recall [46, 139, 140]. It is possible that a drifting-bar gradient visual stimulus may not provide a strong input to the hippocampal network, or the microelectrode tip may be positioned in a region of CA1 that is less responsive to our visual stimulus paradigm. Additionally, considering that pyramidal neurons in CA1 typically exhibit firing rates below 10 Hz [141], it remains unclear whether the observed firing rate within the first week of implantation indicates acute hyperactivity in the network near the microelectrode or a potential bias towards multi-unit activity with similar waveforms. Therefore, future studies exploring firing activity in the hippocampus should employ tetrode for a large-scale SU recording.

Another limitation of this study is the lack of electrochemical characterization for the explanted microelectrode. Performing EIS and cyclic voltammetry during and after explanation could have offered a more comprehensive understanding of the microelectrodes' material integrity and the extent of biological tissue encapsulation [117]. Such insights are crucial for pinpointing the factors that affect the electrophysiological performance of these devices. While this study shows the neuronal loss near the microelectrodes at superficial depths (supplementary figure 3), how tissue reactions may alter the electrical characteristics at the microelectrode contact sites is less explored. Future studies should include detailed characterization of explanted microelectrodes to gain a comprehensive understanding of the instability in recording performance over long implantation periods.

The characterizations of longitudinal changes in the neural network surrounding the implanted microelectrode in our study contribute to the understanding of the instability observed in BCI decoders. However, it is crucial to recognize that tissue responses to a single-shank implanted electrode may differ remarkably from those elicited by 2D multi-shank electrode arrays, such as Utah arrays for clinical BCI applications. Additionally, the reactions of rodent brains in this study are likely to vary from those of non-human primates used in BCI research and humans in clinical applications. There may also be other confounding factors in higher-order subjects. For instance, while BCIs are typically associated with learning in humans and non-human primates [142, 143], distinguishing the effects of long-term implantation injury from those of neuroplasticity-driven learning on neural networks poses a challenge. Furthermore, while one of the potential applications of BCI technology involves using electrical stimulation to treat neurological disorders and restore functional outputs [4, 17], the effects of long-term electrical stimulation on the surrounding neural circuits are not well understood. Electrical stimulation can modulate voltage-gated ion channels, thereby affecting the activity of both neurons and glial cells and may influence the health and functionality of the integrated neural circuit [144–146]. Future research should, therefore, focus on understanding the long-term impacts of electrical stimulation on neural circuits to explore both the beneficial and potentially adverse effects to optimize BCI technologies for therapeutic use.

5. Conclusion

Clinical applications of intracortical microelectrodes face limitations due to decoder instability caused by

plastic learning and network degradation resulting from implantation injury. The chronic instability of the recorded signal's functional network connectivity poses a significant challenge, including the need for regular retraining of the decoder, which consumes substantial time and can be burdensome for patients. To comprehensively understand the impact of implantation injury-related functional degradation, it is crucial to investigate the biological reactions near the chronically implanted microelectrode in conjunction with the degeneration of the functional recording network. In our study, we provide a detailed characterization of changes in functional network activity and synchronization within and across different laminar structures in the cortex and hippocampus. We observed depth-dependent alterations in intralaminar network connectivity with impaired network functionality observed at superficial depths. Furthermore, interlaminar connectivity exhibited direction-dependent changes with reduced connectivity from L2/3 to deeper layers and increased connectivity from L5/6 to superficial depths. These findings contribute to our understanding of the functional responses of the neural network near the microelectrode and shed light on the underlying mechanisms responsible for chronic signal instability and the decline of implanted microelectrodes. By illuminating the intricate dynamics of the functional network and its changes over time, our study paves the way for the design and implementation of more effective interventions to improve the long-term stability and performance of intracortical microelectrodes.

Data availability statement

The data that support the findings of this study are available at the following URL/DOI: www.bioniclab.org. Data will be available from 06 July 2027.

Acknowledgments

This work was supported by: NIH R01NS094396, NIH R01NS105691, NIH R01NS115707, NIH R03AG072218, NIH R01NS129632 and NSF CBET CAREER 1943906.

Author statement

Keying Chen: Conceptualization, Methodology, Validation, Project administration, Data Analysis, Data curation, Investigation, Writing—original draft, review & editing, Revision. **Adam M Forrest**: Writing—review & editing. **Guillermo Gonzalez Burgos**: Writing—review & editing. **Takashi D Y Kozai**: Conceptualization, Resources, Writing—review & editing, Supervision, Funding acquisition

ORCID iD

Takashi D Y Kozai https://orcid.org/0000-0002-2507-3295

References

[1] Shanechi M M 2019 Brain–machine interfaces from motor to mood *Nat. Neurosci.* **22** 1554–64
[2] Vetter R J, Williams J C, Hetke J F, Nunamaker E A and Kipke D R 2004 Chronic neural recording using silicon-substrate microelectrode arrays implanted in cerebral cortex *IEEE Trans. Biomed. Eng.* **51** 896–904
[3] Hochberg L R, Serruya M D, Friehs G M, Mukand J A, Saleh M, Caplan A H, Branner A, Chen D, Penn R D and Donoghue J P 2006 Neuronal ensemble control of prosthetic devices by a human with tetraplegia *Nature* **442** 164–71
[4] Flesher S N, Collinger J L, Foldes S T, Weiss J M, Downey J E, Tyler-Kabara E C, Bensmaia S J, Schwartz A B, Boninger M L and Gaunt R A 2016 Intracortical microstimulation of human somatosensory cortex *Sci. Trans. Med.* **8** 361ra141
[5] Colachis S C, Dunlap C F, Annetta N V, Tamrakar S M, Bockbrader M A and Friedenberg D A 2021 Long-term intracortical microelectrode array performance in a human: a 5 year retrospective analysis *J. Neural Eng.* **18** 0460d7
[6] Michelson N J, Eles J R, Vazquez A L, Ludwig K A and Kozai T D Y 2018 Calcium activation of cortical neurons by continuous electrical stimulation: frequency-dependence, temporal fidelity and activation density *J. Neurosci. Res.* **97** 620–38
[7] Michelson N J and Kozai T D 2018 Isoflurane and ketamine differentially influence spontaneous and evoked laminar electrophysiology in mouse V1 *J. Neurophysiol.* **120** 2232–45
[8] Iordanova B, Vazquez A L, Kozai T D Y, Fukuda M and Kim S G 2018 Optogenetic investigation of the variable neurovascular coupling along the interhemispheric circuits *J. Cereb. Blood Flow Metab.* **38** 627–40
[9] Kozai T D Y, Li X, Bodily L M, Caparosa E M, Zenonos G A, Carlisle D L, Friedlander R M and Cui X T 2014 Effects of caspase-1 knockout on chronic neural recording quality and longevity: insight into cellular and molecular mechanisms of the reactive tissue response *Biomaterials* **35** 9620–34
[10] Flesher S N, Downey J E, Weiss J M, Hughes C L, Herrera A J, Tyler-Kabara E C, Boninger M L, Collinger J L and Gaunt R A 2021 A brain-computer interface that evokes tactile sensations improves robotic arm control *Science* **372** 831–6
[11] Kim S, Callier T, Tabot G A, Gaunt R A, Tenore F V and Bensmaia S J 2015 Behavioral assessment of sensitivity to intracortical microstimulation of primate somatosensory cortex *Proc. Natl Acad. Sci. USA* **112** 15202–7
[12] Hughes C L, Flesher S N, Weiss J M, Boninger M, Collinger J L and Gaunt R A 2021 Perception of microstimulation frequency in human somatosensory cortex *eLife* **10** e65128
[13] Jarosiewicz B, Sarma A A, Bacher D, Masse N Y, Simeral J D, Sorice B, Oakley E M, Blabe C, Pandarinath C and Gilja V 2015 Virtual typing by people with tetraplegia using a self-calibrating intracortical brain-computer interface *Sci. Trans. Med.* **7** 313ra179
[14] Orsborn A L, Moorman H G, Overduin S A, Shanechi M M, Dimitrov D F and Carmena J M 2014 Closed-loop decoder adaptation shapes neural plasticity for skillful neuroprosthetic control *Neuron* **82** 1380–93

[15] Lansdell B, Milovanovic I, Mellema C, Fetz E E, Fairhall A L and Moritz C T 2019 Reconfiguring motor circuits for a joint manual and BCI task *IEEE Trans. Neural Syst. Rehabil. Eng.* **28** 248–57
[16] Perge J A, Homer M L, Malik W Q, Cash S, Eskandar E, Friehs G, Donoghue J P and Hochberg L R 2013 Intra-day signal instabilities affect decoding performance in an intracortical neural interface system *J. Neural Eng.* **10** 036004
[17] Collinger J L, Wodlinger B, Downey J E, Wang W, Tyler-Kabara E C, Weber D J, McMorland A J, Velliste M, Boninger M L and Schwartz A B 2013 High-performance neuroprosthetic control by an individual with tetraplegia *Lancet* **381** 557–64
[18] Zhou X, Tien R N, Ravikumar S and Chase S M 2019 Distinct types of neural reorganization during long-term learning *J. Neurophysiol.* **121** 1329–41
[19] Oby E R, Golub M D, Hennig J A, Degenhart A D, Tyler-Kabara E C, Yu B M, Chase S M and Batista A P 2019 New neural activity patterns emerge with long-term learning *Proc. Natl Acad. Sci.* **116** 15210–5
[20] Athalye V R, Ganguly K, Costa R M and Carmena J M 2017 Emergence of coordinated neural dynamics underlies neuroprosthetic learning and skillful control *Neuron* **93** 955–70.e5
[21] Hochberg L R *et al* 2012 Reach and grasp by people with tetraplegia using a neurally controlled robotic arm *Nature* **485** 372–5
[22] Wodlinger B, Downey J E, Tyler-Kabara E C, Schwartz A B, Boninger M L and Collinger J L 2015 Ten-dimensional anthropomorphic arm control in a human brain-machine interface: difficulties, solutions, and limitations *J. Neural Eng.* **12** 016011
[23] Ajiboye A B, Willett F R, Young D R, Memberg W D, Murphy B A, Miller J P, Walter B L, Sweet J A, Hoyen H A and Keith M W 2017 Restoration of reaching and grasping movements through brain-controlled muscle stimulation in a person with tetraplegia: a proof-of-concept demonstration *Lancet* **389** 1821–30
[24] Silversmith D B, Abiri R, Hardy N F, Natraj N, Tu-Chan A, Chang E F and Ganguly K 2021 Plug-and-play control of a brain–computer interface through neural map stabilization *Nat. Biotechnol.* **39** 326–35
[25] Barrese J C, Rao N, Paroo K, Triebwasser C, Vargas-Irwin C, Franquemont L and Donoghue J P 2013 Failure mode analysis of silicon-based intracortical microelectrode arrays in non-human primates *J. Neural Eng.* **10** 066014
[26] Kozai T D, Catt K, Li X, Gugel Z V, Olafsson V T, Vazquez A L and Cui X T 2015 Mechanical failure modes of chronically implanted planar silicon-based neural probes for laminar recording *Biomaterials* **37** 25–39
[27] Prasad A, Xue Q-S, Dieme R, Sankar V, Mayrand R C, Nishida T, Streit W J and Sanchez J C 2014 Abiotic-biotic characterization of Pt/Ir microelectrode arrays in chronic implants *Front. Neuroeng.* **7** 2
[28] Kozai T D Y, Jaquins-Gerstl A S, Vazquez A L, Michael A C and Cui X T 2014 Brain tissue responses to neural implants impact signal sensitivity and intervention strategies *ACS Chem. Neurosci.* **6** 48–67
[29] Salatino J W, Ludwig K A, Kozai T D Y and Purcell E K 2017 Glial responses to implanted electrodes in the brain *Nat. BME* **2** 52
[30] Biran R, Martin D C and Tresco P A 2005 Neuronal cell loss accompanies the brain tissue response to chronically implanted silicon microelectrode arrays *Exp. Neurol.* **195** 115–26
[31] Michelson N J, Vazquez A L, Eles J R, Salatino J W, Purcell E K, Williams J J, Cui X T and Kozai T D Y 2018 Multi-scale, multi-modal analysis uncovers complex relationship at the brain tissue-implant neural interface: new emphasis on the biological interface *J. Neural Eng.* **15** 033001
[32] Kozai T D Y, Marzullo T C, Hooi F, Langhals N B, Majewska A K, Brown E B and Kipke D R 2010 Reduction of neurovascular damage resulting from microelectrode insertion into the cerebral cortex using in vivo two-photon mapping *J. Neural Eng.* **7** 046011
[33] Johnson M D, Kao O E and Kipke D R 2007 Spatiotemporal pH dynamics following insertion of neural microelectrode arrays *J. Neurosci. Methods* **160** 276–87
[34] Bjornsson C, Oh S J, Al-Kofahi Y, Lim Y, Smith K, Turner J, De S, Roysam B, Shain W and Kim S 2006 Effects of insertion conditions on tissue strain and vascular damage during neuroprosthetic device insertion *J. Neural Eng.* **3** 196
[35] Savya S P, Li F, Lam S, Wellman S M, Stieger K C, Chen K, Eles J R and Kozai T D 2022 In vivo spatiotemporal dynamics of astrocyte reactivity following neural electrode implantation *Biomaterials* **289** 121784
[36] Kozai T D Y, Vazquez A L, Weaver C L, Kim S-G and Cui X T 2012 In vivo two-photon microscopy reveals immediate microglial reaction to implantation of microelectrode through extension of processes *J. Neural Eng.* **9** 066001
[37] Wellman S M, Eles J R, Ludwig K A, Seymour J P, Michelson N J, McFadden W E, Vazquez A L and Kozai T D 2018 A materials roadmap to functional neural interface design *Adv. Funct. Mater.* **28** 1701269
[38] Golabchi A, Wu B, Li X, Carlisle D L, Kozai T D Y, Friedlander R M and Cui X T 2018 Melatonin improves quality and longevity of chronic neural recording *Biomaterials* **180** 225–39
[39] Potter K A, Buck A C, Self W K and Capadona J R 2012 Stab injury and device implantation within the brain results in inversely multiphasic neuroinflammatory and neurodegenerative responses *J. Neural Eng.* **9** 046020
[40] Steven L L, Wellman M, Yaxiaer Y, McNamara I N and Kozai T D 2019 Revealing spatial and temporal patterns of cell death, glial proliferation, and blood-brain barrier dysfunction around implanted intracortical neural interfaces *Front. Neurosci.* **13** 493
[41] Chen K, Wellman S M, Yaxiaer Y, Eles J R and Kozai T D Y 2021 In vivo spatiotemporal patterns of oligodendrocyte and myelin damage at the neural electrode interface *Biomaterials* **268** 120526
[42] Wellman S M, Guzman K, Stieger K C, Brink L E, Sridhar S, Dubaniewicz M T, Li L, Cambi F and Kozai T D Y 2020 Cuprizone-induced oligodendrocyte loss and demyelination impairs recording performance of chronically implanted neural interfaces *Biomaterials* **239** 119842
[43] Chen K, Cambi F and Kozai T D Y 2023 Pro-myelinating clemastine administration improves recording performance of chronically implanted microelectrodes and nearby neuronal health *Biomaterials* **301** 122210
[44] Bassett D S and Gazzaniga M S 2011 Understanding complexity in the human brain *Trends Cogn. Sci.* **15** 200–9
[45] Grillner S, Markram H, De Schutter E, Silberberg G and LeBeau F E N 2005 Microcircuits in action—from CPGs to neocortex *Trends Neurosci.* **28** 525–33
[46] Lee A, Yeung L-K and Barense M 2012 The hippocampus and visual perception *Front. Hum. Neurosci.* **6** 91
[47] Dichter M A and Ayala G F 1987 Cellular mechanisms of epilepsy: a status report *Science* **237** 157–64
[48] Salatino J W, Winter B M, Drazin M H and Purcell E K 2017 Functional remodeling of subtype-specific markers surrounding implanted neuroprostheses *J. Neurophysiol.* **118** 194–202
[49] Schomburg E W, Fernández-Ruiz A, Mizuseki K, Berényi A, Anastassiou C A, Koch C and Buzsáki G 2014 Theta phase segregation of input-specific gamma patterns in entorhinal-hippocampal networks *Neuron* **84** 470–85
[50] Herreras O 2016 Local Field Potentials: myths and misunderstandings *Front. Neural Circuits* **10** 101

[51] Okun M, Naim A and Lampl I 2010 The subthreshold relation between cortical local field potential and neuronal firing unveiled by intracellular recordings in awake rats *J. Neurosci.* **30** 4440
[52] Tort A B L, Komorowski R, Eichenbaum H and Kopell N 2010 Measuring phase-amplitude coupling between neuronal oscillations of different frequencies *J. Neurophysiol.* **104** 1195–210
[53] Scheffer-Teixeira R and Tort A B L 2016 On cross-frequency phase-phase coupling between theta and gamma oscillations in the hippocampus *eLife* **5** e20515
[54] Denker M, Roux S, Lindén H, Diesmann M, Riehle A and Grün S 2011 The local field potential reflects surplus spike synchrony *Cereb. Cortex* **21** 2681–95
[55] Senzai Y, Fernandez-Ruiz A and Buzsáki G 2019 Layer-specific physiological features and interlaminar interactions in the primary visual cortex of the mouse *Neuron* **101** 500–13.e5
[56] Koch P F, Cottone C, Adam C D, Ulyanova A V, Russo R J, Weber M T, Arena J D, Johnson V E and Wolf J A 2020 Traumatic brain injury preserves firing rates but disrupts laminar oscillatory coupling and neuronal entrainment in hippocampal CA1 *Eneuro* **7** ENEURO.0495–19.2020
[57] Berens P 2009 CircStat: a MATLAB toolbox for circular statistics *J. Stat. Softw.* **31** 1–21
[58] Ludwig K A, Miriani R M, Langhals N B, Joseph M D, Anderson D J and Kipke D R 2009 Using a common average reference to improve cortical neuron recordings from microelectrode arrays *J. Neurophysiol.* **101** 1679–89
[59] Stett A, Egert U, Guenther E, Hofmann F, Meyer T, Nisch W and Haemmerle H 2003 Biological application of microelectrode arrays in drug discovery and basic research *Anal. Bioanal. Chem.* **377** 486–95
[60] Tseng H-A and Han X 2021 Distinct spiking patterns of excitatory and inhibitory neurons and LFP oscillations in prefrontal cortex during sensory discrimination *Front. Physiol.* **12** 101
[61] Csicsvari J, Hirase H, Czurkó A, Mamiya A and Buzsáki G 1999 Oscillatory coupling of hippocampal pyramidal cells and interneurons in the behaving rat *J. Neurosci.* **19** 274
[62] Moradi Chameh H, Rich S, Wang L, Chen F-D, Zhang L, Carlen P L, Tripathy S J and Valiante T A 2021 Diversity amongst human cortical pyramidal neurons revealed via their sag currents and frequency preferences *Nat. Commun.* **12** 2497
[63] Mizuseki K, Royer S, Diba K and Buzsáki G 2012 Activity dynamics and behavioral correlates of CA3 and CA1 hippocampal pyramidal neurons *Hippocampus* **22** 1659–80
[64] Bruno R M and Sakmann B 2006 Cortex is driven by weak but synchronously active thalamocortical synapses *Science* **312** 1622–7
[65] Chmielowska J, Carvell G E and Simons D J 1989 Spatial organization of thalamocortical and corticothalamic projection systems in the rat SmI barrel cortex *J. Comp. Neurol.* **285** 325–38
[66] Tremblay R, Lee S and Rudy B 2016 GABAergic interneurons in the neocortex: from cellular properties to circuits *Neuron* **91** 260–92
[67] Ascoli G A *et al* 2008 The petilla interneuron nomenclature, petilla terminology: nomenclature of features of GABAergic interneurons of the cerebral cortex *Nat. Rev. Neurosci.* **9** 557–68
[68] Harris K D, Quiroga R Q, Freeman J and Smith S L 2016 Improving data quality in neuronal population recordings *Nat. Neurosci.* **19** 1165–74
[69] Buzsáki G 2004 Large-scale recording of neuronal ensembles *Nat. Neurosci.* **7** 446–51
[70] Buzsáki G, Anastassiou C A and Koch C 2012 The origin of extracellular fields and currents—EEG, ECoG, LFP and spikes *Nat. Rev. Neurosci.* **13** 407–20
[71] Poulet J F A and Petersen C C H 2008 Internal brain state regulates membrane potential synchrony in barrel cortex of behaving mice *Nature* **454** 881–5
[72] Lisman J E and Jensen O 2013 The theta-gamma neural code *Neuron* **77** 1002–16
[73] Scheffer-Teixeira R, Belchior H, Caixeta F V, Souza B C, Ribeiro S and Tort A B L 2012 Theta phase modulates multiple layer-specific oscillations in the CA1 region *Cereb. Cortex* **22** 2404–14
[74] Gilbert C D and Wiesel T N 1979 Morphology and intracortical projections of functionally characterised neurones in the cat visual cortex *Nature* **280** 120–5
[75] Buzsáki G and Wang X-J 2012 Mechanisms of gamma oscillations *Annu. Rev. Neurosci.* **35** 203–25
[76] Baker A, Kalmbach B, Morishima M, Kim J, Juavinett A, Li N and Dembrow N 2018 Specialized subpopulations of deep-layer pyramidal neurons in the neocortex: bridging cellular properties to functional consequences *J. Neurosci.* **38** 5441
[77] Keller D, Erö C and Markram H 2018 Cell Densities in the mouse brain: a systematic review *Front. Neuroanat.* **12** 83
[78] Quiquempoix M, Fayad S L, Boutourlinsky K, Leresche N, Lambert R C and Bessaih T 2018 Layer 2/3 pyramidal neurons control the gain of cortical output *Cell Rep.* **24** 2799–807.e4
[79] Parkis M A, Feldman J L, Robinson D M and Funk G D 2003 Oscillations in endogenous inputs to neurons affect excitability and signal processing *J. Neurosci.* **23** 8152
[80] Roach J P, Pidde A, Katz E, Wu J, Ognjanovski N, Aton S J and Zochowski M R 2018 Resonance with subthreshold oscillatory drive organizes activity and optimizes learning in neural networks *Proc. Natl Acad. Sci.* **115** E3017–25
[81] DeFelipe J *et al* 2013 New insights into the classification and nomenclature of cortical GABAergic interneurons *Nat. Rev. Neurosci.* **14** 202–16
[82] Gerfen C R, Economo M N and Chandrashekar J 2018 Long distance projections of cortical pyramidal neurons *J. Neurosci. Res.* **96** 1467–75
[83] Harris K D and Shepherd G M G 2015 The neocortical circuit: themes and variations *Nat. Neurosci.* **18** 170–81
[84] Douglas R J and Martin K A C 2004 Neuronal circuits of the neocortex *Ann. Rev. Neurosci.* **27** 419–51
[85] Kim E J, Juavinett A L, Kyubwa E M, Jacobs M W and Callaway E M 2015 Three types of cortical layer 5 neurons that differ in brain-wide connectivity and function *Neuron* **88** 1253–67
[86] Hage T A, Bosma-Moody A, Baker C A, Kratz M B, Campagnola L, Jarsky T, Zeng H and Murphy G J 2022 Synaptic connectivity to L2/3 of primary visual cortex measured by two-photon optogenetic stimulation *eLife* **11** e71103
[87] Shepherd G M G and Svoboda K 2005 Laminar and columnar organization of ascending excitatory projections to layer 2/3 pyramidal neurons in rat barrel cortex *J. Neurosci.* **25** 5670
[88] Shepherd G M G, Stepanyants A, Bureau I, Chklovskii D and Svoboda K 2005 Geometric and functional organization of cortical circuits *Nat. Neurosci.* **8** 782–90
[89] Yoshimura Y, Dantzker J L M and Callaway E M 2005 Excitatory cortical neurons form fine-scale functional networks *Nature* **433** 868–73
[90] Debnath S, Prins N W, Pohlmeyer E, Mylavarapu R, Geng S, Sanchez J C and Prasad A 2018 Long-term stability of neural signals from microwire arrays implanted in common marmoset motor cortex and striatum *Biomed. Phys. Eng. Express* **4** 055025
[91] Chestek C A *et al* 2011 Long-term stability of neural prosthetic control signals from silicon cortical arrays in rhesus macaque motor cortex *J. Neural Eng.* **8** 045005
[92] Degenhart A D, Bishop W E, Oby E R, Tyler-Kabara E C, Chase S M, Batista A P and Yu B M 2020 Stabilization of a brain–computer interface via the alignment of low-dimensional spaces of neural activity *Nat. Biomed. Eng.* **4** 672–85
[93] Downey J E, Schwed N, Chase S M, Schwartz A B and Collinger J L 2018 Intracortical recording stability in

human brain–computer interface users *J. Neural Eng.* **15** 046016
[94] Peron S, Pancholi R, Voelcker B, Wittenbach J D, Ólafsdóttir H F, Freeman J and Svoboda K 2020 Recurrent interactions in local cortical circuits *Nature* **579** 256–9
[95] Gao W-J, Yang -S-S, Mack N R and Chamberlin L A 2022 Aberrant maturation and connectivity of prefrontal cortex in schizophrenia—contribution of NMDA receptor development and hypofunction *Mol. Psychiatry* **27** 731–43
[96] Aponte D A, Handy G, Kline A M, Tsukano H, Doiron B and Kato H K 2021 Recurrent network dynamics shape direction selectivity in primary auditory cortex *Nat. Commun.* **12** 314
[97] Ayata P and Schaefer A 2020 Innate sensing of mechanical properties of brain tissue by microglia *Curr. Opin. Immunol.* **62** 123–30
[98] Costello D A, Lyons A, Denieffe S, Browne T C, Cox F F and Lynch M A 2011 Long term potentiation is impaired in membrane glycoprotein CD200-deficient mice: a role for Toll-like receptor activation * *J. Biol. Chem.* **286** 34722–32
[99] Dzyubenko E, Fleischer M, Manrique-Castano D, Borbor M, Kleinschnitz C, Faissner A and Hermann D M 2021 Inhibitory control in neuronal networks relies on the extracellular matrix integrity *Cell. Mol. Life Sci.* **78** 5647–63
[100] Buzsáki G, Kaila K and Raichle M 2007 Inhibition and brain work *Neuron* **56** 771–83
[101] Kee T, Sanda P, Gupta N, Stopfer M and Bazhenov M 2015 Feed-forward versus feedback inhibition in a basic olfactory circuit *PLoS Comput. Biol.* **11** e1004531
[102] Tetzlaff T, Helias M, Einevoll G T and Diesmann M 2012 Decorrelation of neural-network activity by inhibitory feedback *PLoS Comput. Biol.* **8** e1002596
[103] McCafferty C *et al* 2018 Cortical drive and thalamic feed-forward inhibition control thalamic output synchrony during absence seizures *Nat. Neurosci.* **21** 744–56
[104] Fazzari P, Mortimer N, Yabut O, Vogt D and Pla R 2020 Cortical distribution of GABAergic interneurons is determined by migration time and brain size *Development* **147** dev185033
[105] Adams D L, Piserchia V, Economides J R and Horton J C 2015 Vascular supply of the cerebral cortex is specialized for cell layers but not columns *Cereb. Cortex* **25** 3673–81
[106] Schmid F, Barrett M J P, Jenny P and Weber B 2019 Vascular density and distribution in neocortex *Neuroimage* **197** 792–805
[107] Agarwal N and Carare R O 2021 Cerebral vessels: an overview of anatomy, physiology, and role in the drainage of fluids and solutes *Front. Neurol.* **11** 611485
[108] Figley C R and Stroman P W 2011 The role(s) of astrocytes and astrocyte activity in neurometabolism, neurovascular coupling, and the production of functional neuroimaging signals *Eur. J. Neurosci.* **33** 577–88
[109] Stackhouse T L and Mishra A 2021 Neurovascular coupling in development and disease: focus on astrocytes *Front. Cell Dev. Biol.* **9** 702832
[110] McConnell G C, Rees H D, Levey A I, Gutekunst C-A, Gross R E and Bellamkonda R V 2009 Implanted neural electrodes cause chronic, local inflammation that is correlated with local neurodegeneration *J. Neural Eng.* **6** 056003
[111] Tomassy G S, Berger D R, Chen H-H, Kasthuri N, Hayworth K J, Vercelli A, Seung H S, Lichtman J W and Arlotta P 2014 Distinct profiles of myelin distribution along single axons of pyramidal neurons in the neocortex *Science* **344** 319–24
[112] Brown G C and Neher J J 2012 Eaten alive! Cell death by primary phagocytosis: 'phagoptosis *Trends Biochem. Sci.* **37** 325–32
[113] Sierra A, Abiega O, Shahraz A and Neumann H 2013 Janus-faced microglia: beneficial and detrimental consequences of microglial phagocytosis *Front. Cell. Neurosci.* **7** 6
[114] Tang Y and Le W 2016 Differential roles of M1 and M2 microglia in neurodegenerative diseases *Mol. Neurobiol.* **53** 1181–94
[115] Fu R, Shen Q, Xu P, Luo J J and Tang Y 2014 Phagocytosis of microglia in the central nervous system diseases *Mol. Neurobiol.* **49** 1422–34
[116] Wellman S M and Kozai T D Y 2018 *In vivo* spatiotemporal dynamics of NG2 glia activity caused by neural electrode implantation *Biomaterials* **164** 121–33
[117] Woeppel K, Hughes C, Herrera A J, Eles J R, Tyler-Kabara E C, Gaunt R A, Collinger J L and Cui X T 2021 Explant analysis of Utah electrode arrays implanted in human cortex for brain-computer-interfaces *Front. Bioeng. Biotechnol.* **9** 759711
[118] Cody P A, Eles J R, Lagenaur C F, Kozai T D Y and Cui X T 2018 Unique electrophysiological and impedance signatures between encapsulation types: an analysis of biological Utah array failure and benefit of a biomimetic coating in a rat model *Biomaterials* **161** 117–28
[119] Patel P R *et al* 2023 Utah array characterization and histological analysis of a multi-year implant in non-human primate motor and sensory cortices *J. Neural Eng.* **20** 014001
[120] Bennett C, Samikkannu M, Mohammed F, Dietrich W D, Rajguru S M and Prasad A 2018 Blood brain barrier (BBB)-disruption in intracortical silicon microelectrode implants *Biomaterials* **164** 1–10
[121] Rousche P J and Normann R A 1998 Chronic recording capability of the Utah intracortical electrode array in cat sensory cortex *J. Neurosci. Methods* **82** 1–15
[122] Campbell A and Wu C 2018 Chronically implanted intracranial electrodes: tissue reaction and electrical changes *Micromachines* **9** 430
[123] Chen K, Stieger K C and Kozai T D Y 2021 Challenges and opportunities of advanced gliomodulation technologies for excitation-inhibition balance of brain networks *Curr. Opin. Biotechnol.* **72** 112–20
[124] Badimon A *et al* 2020 Negative feedback control of neuronal activity by microglia *Nature* **586** 417–23
[125] Cserép C *et al* 2020 Microglia monitor and protect neuronal function through specialized somatic purinergic junctions *Science* **367** 528
[126] Yu X, Taylor A M W, Nagai J, Golshani P, Evans C J, Coppola G and Khakh B S 2018 Reducing astrocyte calcium signaling in vivo alters striatal microcircuits and causes repetitive behavior *Neuron* **99** 1170–87.e9
[127] Kwak H *et al* 2020 Astrocytes control sensory acuity via tonic inhibition in the thalamus *Neuron* **108** 691–706.e10
[128] Zou C, Shi Y, Ohli J, Schüller U, Dorostkar M M and Herms J 2016 Neuroinflammation impairs adaptive structural plasticity of dendritic spines in a preclinical model of Alzheimer's disease *Acta Neuropathol.* **131** 235–46
[129] Xie C, Zhang Q, Ye X, Wu W, Cheng X, Ye X, Ruan J and Pan X 2023 Periodontitis-induced neuroinflammation impacts dendritic spine immaturity and cognitive impairment *Oral Dis.* **30** 2558–69
[130] Morrison B M, Lee Y and Rothstein J D 2013 Oligodendroglia: metabolic supporters of axons *Trends Cell Biol.* **23** 644–51
[131] Nave K-A and Werner H B 2014 Myelination of the nervous system: mechanisms and functions *Annu. Rev. Cell Dev. Biol.* **30** 503–33
[132] Moore S *et al* 2020 A role of oligodendrocytes in information processing *Nat. Commun.* **11** 5497
[133] Xin W, Mironova Y A, Shen H, Marino R A M, Waisman A, Lamers W H, Bergles D E and Bonci A 2019 Oligodendrocytes support neuronal glutamatergic transmission via expression of glutamine synthetase *Cell Rep.* **27** 2262–71.e5
[134] Pepper R E, Pitman K A, Cullen C L and Young K M 2018 How do cells of the oligodendrocyte lineage affect neuronal circuits to influence motor function, memory and mood? *Front. Cell. Neurosci.* **12** 399

[135] Ereifej E S, Smith C S, Meade S M, Chen K, Feng H and Capadona J R 2018 The neuroinflammatory response to nanopatterning parallel grooves into the surface structure of intracortical microelectrodes *Adv. Funct. Mater.* **28** 1704420
[136] Becchetti A, Gullo F, Bruno G, Dossi E, Lecchi M and Wanke E 2012 Exact distinction of excitatory and inhibitory neurons in neural networks: a study with GFP-GAD67 neurons optically and electrophysiologically recognized on multielectrode arrays *Front. Neural Circuits* **6** 63
[137] Judit M V, Tibor A, Petra N-P and Norbert H 2023 CaMKIIα promoter-controlled circuit manipulations target both pyramidal cells and inhibitory interneurons in cortical networks *Eneuro* **10** ENEURO.0070–23.2023
[138] Gray C M, Maldonado P E, Wilson M and McNaughton B 1995 Tetrodes markedly improve the reliability and yield of multiple single-unit isolation from multi-unit recordings in cat striate cortex *J. Neurosci. Methods* **63** 43–54
[139] Kim S, Jeneson A, van der Horst A S, Frascino J C, Hopkins R O and Squire L R 2011 Memory, visual discrimination performance, and the human hippocampus *J. Neurosci.* **31** 2624
[140] Aly M, Ranganath C and Yonelinas A P 2013 Detecting changes in scenes: the hippocampus is critical for strength-based perception *Neuron* **78** 1127–37
[141] Mizuseki K and Buzsáki G 2013 Preconfigured, skewed distribution of firing rates in the hippocampus and entorhinal cortex *Cell Rep.* **4** 1010–21
[142] Carelli L *et al* 2017 Brain-computer interface for clinical purposes: cognitive assessment and rehabilitation *Biomed. Res. Int.* **2017** 1695290
[143] Nuyujukian P, Kao J C, Ryu S I and Shenoy K V 2017 A nonhuman primate brain–computer typing interface *Proc. IEEE* **105** 66–72
[144] Michelle L O, Baljit S K, Serguei N S, Min Z, Lee C J and Nathalie R 2015 New insights on astrocyte ion channels: critical for homeostasis and neuron-glia signaling *J. Neurosci.* **35** 13827
[145] Schlick B, Flucher B E and Obermair G J 2010 Voltage-activated calcium channel expression profiles in mouse brain and cultured hippocampal neurons *Neuroscience* **167** 786–98
[146] Izquierdo P, Attwell D and Madry C 2019 Ion channels and receptors as determinants of microglial function *Trends Neurosci.* **42** 278–92